





ARTICLE

The minus-end depolymerase KIF2A drives flux-like treadmilling of γ TuRC-uncapped microtubules

Gil Henkin^{1*} , Cláudia Brito^{1*} , Claire Thomas² , and Thomas Surrey^{1,3,4} 

During mitosis, microtubules in the spindle turn over continuously. At spindle poles, where microtubule minus ends are concentrated, microtubule nucleation and depolymerization, the latter required for poleward microtubule flux, happen side by side. How these seemingly antagonistic processes of nucleation and depolymerization are coordinated is not understood. Here, we reconstitute this coordination *in vitro* combining different pole-localized activities. We find that the spindle pole-localized kinesin-13 KIF2A is a microtubule minus-end depolymerase, in contrast to its paralog MCAK. Due to its asymmetric activity, KIF2A still allows microtubule nucleation from the γ -tubulin ring complex (γ TuRC), which serves as a protective cap shielding the minus end against KIF2A binding. Efficient γ TuRC uncapping requires the combined action of KIF2A and a microtubule severing enzyme, leading to treadmilling of the uncapped microtubule driven by KIF2A. Together, these results provide insight into the molecular mechanisms by which a minimal protein module coordinates microtubule nucleation and depolymerization at spindle poles consistent with their role in poleward microtubule flux.

Introduction

The microtubule cytoskeleton is essential for a multitude of processes in eukaryotic cells, such as intracellular organization and trafficking, cell division, and differentiation. Microtubules are structurally polar filaments with two biochemically distinct ends with characteristic differences in their dynamic properties that are critical for microtubule function (Akhmanova and Steinmetz, 2015; Gudimchuk and McIntosh, 2021). Both ends of microtubules can switch stochastically between episodes of growth and shrinkage, a property called dynamic instability, which is ultimately a consequence of GTP hydrolysis at the microtubule end (Desai and Mitchison, 1997; Mitchison and Kirschner, 1984). The dynamic properties of microtubule plus ends and their regulation have been extensively studied, both in cells and also *in vitro* with purified proteins, but much less is known about the regulation of microtubule minus-end dynamics (Akhmanova and Steinmetz, 2019).

Across eukaryotic cells, major microtubule nucleation pathways require the γ -tubulin ring complex (γ TuRC), a large multisubunit protein complex that serves as a template for microtubule formation (Kollman et al., 2011; Tovey and Conduit, 2018). Nucleation from purified γ TuRC *in vitro* results in microtubules with stably γ TuRC-capped minus ends and dynamic plus ends (Berman et al., 2023; Consolati et al., 2020; Rai et al., 2022 Preprint; Thawani et al., 2020; Wieczorek et al., 2021). To what

extent γ TuRC-nucleated microtubule minus ends remain capped in cells is not clear, and recent electron microscopy data suggests there is a mixture of capped and uncapped minus ends in cells (Kiewisz et al., 2022; Laguillo-Diego et al., 2023).

In mitotic and meiotic spindles during cell division, microtubule minus ends at the spindle poles appear to slowly depolymerize while dynamic microtubule plus ends in the spindle center display net polymerization, leading to a constant flux of microtubule mass from the spindle center to its poles (Barisic et al., 2021; Cameron et al., 2006; Ferenz and Wadsworth, 2007; Ganem et al., 2005; Mitchison, 1989; Risteski et al., 2022; Rogers et al., 2005; Steblyanko et al., 2020). How microtubule minus-end dynamics at spindle poles are regulated during poleward flux remains a major open question. On one hand, γ TuRC is enriched at spindle poles, in agreement with the poles' microtubule-nucleating properties. On the other hand, a number of microtubule-destabilizing proteins involved in regulating microtubule flux are also known to accumulate at spindle poles, such as the microtubule depolymerase KIF2A, a kinesin-13 (Gaetz and Kapoor, 2004; Ganem and Compton, 2004; Welburn and Cheeseman, 2012), and the microtubule severases, like katanin, fidgetin, and spastin (Jiang et al., 2017; McNally et al., 1996; Zhang et al., 2007). The molecular mechanism by which this mixture of seemingly antagonistic microtubule

¹Centre for Genomic Regulation (CRG), Barcelona Institute of Science and Technology (BIST), Barcelona, Spain; ²The Francis Crick Institute, London, UK; ³Universitat Pompeu Fabra (UPF), Barcelona, Spain; ⁴ICREA, Barcelona, Spain.

*G. Henkin and C. Brito contributed equally to this paper. Correspondence to Thomas Surrey: thomas.surrey@crg.eu

G. Henkin's current affiliation is Max Planck Institute for Infection Biology, Berlin, Germany.

© 2023 Henkin et al. This article is available under a Creative Commons License (Attribution 4.0 International, as described at <https://creativecommons.org/licenses/by/4.0/>).

nucleating and destabilizing activities at the spindle pole can control microtubule minus-end dynamics to ensure correct microtubule flux and hence correct spindle function is unknown.

The kinesin-13s are not directionally motile, but instead bind microtubules in a diffusive manner and depolymerize them from their ends. This function requires ATPase activity as well as the positively-charged and class-specific “neck,” which is directly N-terminal to the conserved kinesin motor domain (Desai et al., 1999; Ems-McClung and Walczak, 2010; Friel and Welburn, 2018; Moores and Milligan, 2006). The N- and C-termini of the kinesin-13s drive cellular localization and homodimerization, respectively (Maney et al., 2001; Welburn and Cheeseman, 2012). In the ATP state, both the neck and motor domains bind two longitudinally bound tubulin dimers in a bent conformation, which suggests an “unpeeling” mechanism to remove tubulin from microtubule ends (Benoit et al., 2018; Trofimova et al., 2018; Wang et al., 2017).

The majority of kinesin-13 studies have focused on MCAK (KIF2C), which preferentially localizes to kinetochores in cells and is involved in the correct chromosome–spindle attachment (Ganem et al., 2005; Manning et al., 2007; Welburn and Cheeseman, 2012; Wordeman et al., 2007). In vitro, purified MCAK slowly depolymerizes both ends of artificially stabilized microtubules at similar speeds and promotes the transition from growth to fast shrinkage, called catastrophe, of dynamic microtubules (Desai et al., 1999; Gardner et al., 2011; Montenegro Gouveia et al., 2010). The paralog KIF2A, on the other hand, localizes mainly at spindle poles, and is important for correct spindle architecture and length, promoting poleward flux (Gaetz and Kapoor, 2004; Ganem and Compton, 2004; Steblyanko et al., 2020; Uehara et al., 2013; Wilbur and Heald, 2013). Although KIF2A has been studied less in vitro (Desai et al., 1999; Wilbur and Heald, 2013), it is thought that KIF2A and MCAK share identical enzymatic activities, with their functional differences in cells resulting from different localizations mediated by specific binding partners. It is however still unknown how KIF2A contributes to the control of microtubule minus-end dynamics at spindle poles, especially given that most minus ends at spindle poles are expected to be capped after having been nucleated by γ TuRCs.

Microtubule uncapping by microtubule severases could allow KIF2A to depolymerize minus ends at spindle poles (Sharp and Ross, 2012; Zhang et al., 2007), and indeed severases promote poleward flux (Guerreiro et al., 2021; Huang et al., 2021). They are hexameric AAA proteins that pull on the negatively charged C-terminal tails of tubulin on the microtubule lattice, inducing damage that can lead to microtubule severing, exposing new plus and minus ends (Roll-Mecak and Vale, 2008; Zehr et al., 2020). This process has however been shown to be inefficient in the presence of soluble tubulin due to spontaneous re-incorporation of tubulin at the damage sites (Jiang et al., 2017; Vemu et al., 2018), raising the question of how efficient minus-end uncapping by severases could be at the spindle poles. The molecular mechanisms of how γ TuRC, KIF2A, and severases in combination control microtubule minus-end dynamics to ensure correct spindle function remain largely unknown.

Here, we demonstrate that KIF2A is an inherently asymmetric microtubule depolymerase. It preferentially binds to and depolymerizes the minus ends of microtubules, in agreement with its function in the spindle, and is distinct from the symmetric behavior of its paralog MCAK. KIF2A alone is sufficient to induce microtubule treadmilling that recapitulates poleward flux by slowly depolymerizing the minus ends of dynamic microtubules while permitting plus-end growth. We find that KIF2A still allows microtubule nucleation by γ TuRC and that γ TuRC capping of minus ends interferes with KIF2A-mediated minus end depolymerization. The severase spastin and KIF2A are together required to create fresh minus ends via active γ TuRC-uncapping and to induce KIF2A-mediated microtubule treadmilling. Altogether, our results provide new insight into the molecular mechanism of the control of microtubule minus-end dynamics by the γ TuRC/KIF2A/severase module, consistent with their role at spindle poles during cell division.

Results

KIF2A is a microtubule minus-end depolymerase

We expressed and purified the human kinesin-13 KIF2A fused to the fluorescent protein mScarlet (mScarlet-KIF2A; Fig. 1 A and Fig. S1 A) and studied its depolymerization activity on microtubules using a total internal reflection fluorescence (TIRF) microscopy-based in vitro assay (Fig. 1 A). We were surprised to observe strongly asymmetric depolymerization of glass-immobilized microtubules that were stabilized using the slowly hydrolyzable GTP analog GMPCPP (Video 1). One microtubule end depolymerized considerably faster than the other (Fig. 1 B), and mScarlet-KIF2A strongly accumulated at the more-quickly shrinking end (Fig. S2 A). This is in contrast to the activity of other kinesin-13s such as MCAK, which display rather symmetric depolymerization activity at both ends of stabilized microtubules (Desai et al., 1999; Helenius et al., 2006; Hunter et al., 2003).

Polarity-labeling of GMPCPP-microtubules showed that mScarlet-KIF2A preferentially bound to and depolymerized microtubule minus ends; plus ends depolymerized between 5 and 10 times more slowly (Fig. 1 C, left, Fig. 1 D). A purified KIF2A construct without a fluorescent tag (Fig. S1 B) showed similar asymmetric depolymerase behavior on polarity-marked GMPCPP microtubules (Fig. S2, B and C). To be able to directly compare the activities of KIF2A and MCAK under the same assay conditions, we expressed and purified MCAK fused to mCherry (mCherry-MCAK; Fig. 1 A and Fig. S1 C) and confirmed that MCAK does not have a minus end preference, neither for accumulation nor for depolymerization of GMPCPP microtubules (Fig. 1 C, right; Fig. 1 D).

Varying the mScarlet-KIF2A concentration, we observed that the depolymerization speed of both the minus and the plus end of non-polarity-marked microtubules (distinguished by considering that the minus end depolymerizes faster) increased with the KIF2A concentration, maintaining a strongly asymmetric depolymerization character at all the KIF2A concentrations tested (Fig. 1 E). All in all, this demonstrates that KIF2A is inherently different from MCAK, preferentially depolymerizing

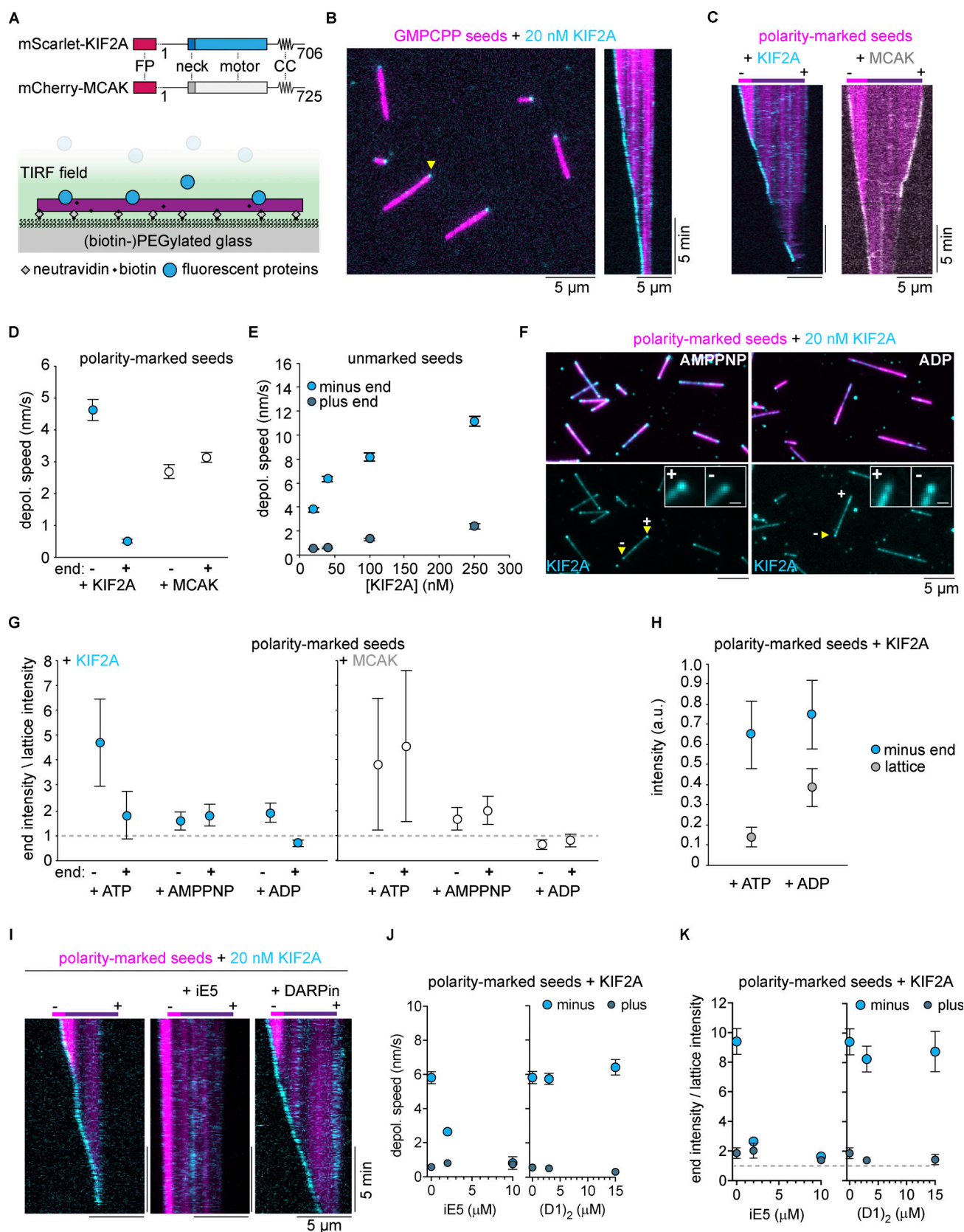


Figure 1. The depolymerase KIF2A preferentially accumulates and depolymerizes the minus ends of microtubules. (A) Schematic of fluorescently tagged KIF2A and MCAK constructs used in this study, indicating the fluorescent protein (FP) fused via a flexible linker to the N-terminus of each protein, the conserved internal motor domain, and the class-specific neck and predicted coiled-coil dimerization domain (CC) N- and C-terminal to the motor domain. Below, schematic of TIRF microscopy experiment set-up. (B) TIRF microscopy image of 20 nM mScarlet-KIF2A (cyan) binding to GMPCPP-microtubule seeds

(AlexaFluor647, 5%; magenta) bound to the glass surface. A kymograph of a depolymerizing microtubule seed indicated by the yellow arrow is on the right. **(C)** Kymographs of GMPCPP-microtubule seeds with a dimly labeled plus end and brightly labeled minus end (AlexaFluor647; magenta) being depolymerized by 20 nM mScarlet-KIF2A (left; cyan) or 20 nM mCherry-MCAK (right; gray). **(D)** Depolymerization rates of each end of polarity-marked GMPCPP seeds by 20 nM mScarlet-KIF2A ($n = 29$ microtubules) and 20 nM mCherry-MCAK ($n = 33$ microtubules). Error bars are SEM. **(E)** Depolymerization rates of GMPCPP-microtubule seeds at varying concentrations of mScarlet-KIF2A. Polarity of the seed was assigned assuming the minus end depolymerizes at the faster rate. Number of microtubule seeds measured per condition: mScarlet-KIF2A: 20 nM, $n = 46$; 40 nM, $n = 61$; 100 nM, $n = 78$; 250 nM, $n = 64$. Error bars are SEM. **(F)** Localization of mScarlet-KIF2A (20 nM) on polarity-marked microtubule seeds in AMPPNP and ADP. Images are averages of 10 frames. Top row: Merged channels (AlexaFluor647 tubulin, magenta; mScarlet-KIF2A, cyan). Bottom row: mScarlet-KIF2A channel alone. Bottom inset: Cropped and enlarged images of mScarlet-KIF2A binding to microtubule ends, showing its localization to both ends in AMPPNP, and its localization to the minus end, and not the plus end, in ADP. Inset scale bars: 1 μm . **(G)** The ratio of intensity of mScarlet-KIF2A or mCherry-MCAK (both 20 nM) at microtubule ends to their intensity on the microtubule lattice (see Materials and methods). A dashed line at a ratio of 1 indicates equal binding to the end and the lattice. Number of microtubule seeds measured per condition: mScarlet-KIF2A: ATP, $n = 26$; AMPPNP, $n = 29$; ADP, $n = 36$; mCherry-MCAK: ATP, $n = 47$; AMPPNP, $n = 40$; ADP, $n = 32$. Error bars are SEM. **(H)** Raw mScarlet-KIF2A intensities at minus ends and on the lattice in ATP and ADP (see Materials and methods). Error bars are SEM. **(I)** Kymographs of polarity-marked GMPCPP seeds (Atto647; magenta) in the presence of 20 nM mScarlet-KIF2A (cyan) and either 2 μM iE5 (middle) or 15 μM (D1)₂ (right). **(J)** Depolymerization speeds of plus and minus ends of polarity-marked GMPCPP seeds in the presence of 20 nM mScarlet-KIF2A ($n = 173$ microtubules) and either iE5 (2 μM , $n = 149$ microtubules; 10 μM , $n = 125$) or (D1)₂ (3 μM , $n = 149$ microtubules; 15 μM , $n = 141$ microtubules). Error bars are SEM. **(K)** Ratio of microtubule end and lattice intensities of mScarlet-KIF2A ($n = 44$ microtubules) in the absence or presence of iE5 (2 μM , $n = 44$ microtubules; 10 μM , $n = 55$) or (D1)₂ (3 μM , $n = 52$ microtubules; 15 μM , $n = 37$ microtubules) at the indicated concentrations. Dashed line indicates equal binding to the end and the lattice (ratio = 1). Error bars are SEM.

minus ends, consistent with its proposed role at spindle poles (Cameron et al., 2006; Gaetz and Kapoor, 2004; Ganem and Compton, 2004).

Kinesin-13s may recognize a particular lattice curvature at microtubule ends induced by ATP binding of the motor domain (Benoit et al., 2018; Desai et al., 1999; Hunter et al., 2003; Trofimova et al., 2018; Wang et al., 2017). Therefore, we asked if also the preferential accumulation of KIF2A at minus ends was dependent on its nucleotide state. We found that mScarlet-KIF2A accumulated at both ends of microtubules in the presence of the non-hydrolyzable ATP analog AMPPNP (Fig. 1 F, left), as observed previously with kinesin-13s (Desai et al., 1999; McHugh et al., 2019; Moores et al., 2002). However, we were surprised to find that in the presence of ADP, KIF2A accumulated only at the minus and not at the plus ends (Fig. 1 F, right). We quantified the extent of end versus lattice accumulation by measuring fluorescence intensity ratios. In the presence of ATP, KIF2A not only showed a marked binding preference for the minus end but also accumulated mildly at the plus end (Fig. 1 G, left, ATP), consistent with the observed difference in depolymerization rates at the two ends. In the presence of AMPPNP, KIF2A accumulated equivalently mildly at both plus and minus ends, remarkably without a minus-end preference (Fig. 1 G, left, AMPPNP), whereas with ADP, KIF2A accumulation only showed a minus-end preference (Fig. 1 G, left, ADP). Because ADP also increased KIF2A's binding to the microtubule lattice (Fig. 1 H), the ratio of end-to-lattice intensity was lower for ADP than ATP, but the amount of KIF2A motors bound to minus ends was similar in the presence of ATP and ADP (Fig. 1 H). Taken together, these results indicate that the selective microtubule minus end accumulation by KIF2A is distinct from the indiscriminate end accumulation of MCAK and that there is a structure at minus ends, and not at plus ends, that KIF2A can recognize independent of ATP binding. In contrast, MCAK did not show any end accumulation in the presence of ADP, whereas it accumulated at both ends equally strongly in ATP and equally mildly in AMPPNP (Fig. 1 G, right), as observed previously (Desai et al., 1999; Helenius et al., 2006; Hertzner et al., 2006; McHugh et al., 2019).

To further investigate the mechanism of minus end recognition by KIF2A, we next purified the microtubule end capping protein iE5 (Fig. S1 D) and DARPIn (D1)₂ (Fig. S1 E), which specifically cap either the minus or the plus ends of microtubules, respectively (Campanacci et al., 2019; Pecqueur et al., 2012). Using polarity-marked microtubules, we observed that while (D1)₂ had no influence on KIF2A's capacity to accumulate at and depolymerize microtubule minus ends, as one would expect, iE5 effectively hindered both minus end accumulation and depolymerization by KIF2A (Fig. 1, I–K). These results suggest that KIF2A might interact with the exposed surface of the α -tubulins that iE5 binds to, suggesting a new model for microtubule minus end recognition by KIF2A.

KIF2A selectively depolymerizes the minus ends of dynamic microtubules

Having established a robust minus-end preference for KIF2A using stabilized microtubules, we next investigated if KIF2A also acts asymmetrically on dynamic microtubules growing from immobilized GMPCPP microtubule seeds in the presence of soluble GTP-tubulin (Fig. 2 A and Video 2). Dynamic microtubule extensions could be distinguished from seeds by including a higher ratio of fluorescent tubulin in the seed (Fig. 2 B). In the absence of mScarlet-KIF2A, the faster-growing microtubule plus ends could easily be distinguished from the more slowly growing minus ends (Fig. 2 B; no KIF2A). Adding mScarlet-KIF2A selectively suppressed minus-end growth already at low concentrations (Fig. 2 B; 2 nM, 5 nM KIF2A) and caused selective minus-end depolymerization of the GMPCPP seed at higher concentrations. At the same time, plus-end growth could be observed up to 100 nM of KIF2A (Fig. 2 B; 20 nM, 100 nM KIF2A) without affecting the plus-end growth speed (Fig. 2 C, top left). The plus-end growth speed was also unaffected by MCAK (Fig. 2 C, top right), in agreement with previous MCAK studies (Gardner et al., 2011; Montenegro Gouveia et al., 2010). At higher concentrations, KIF2A also accumulates along the microtubule lattice, triggering more frequently the transition from plus-end growth to shrinkage, thus increasing the plus-end catastrophe frequency (Fig. 2, B and C, bottom left).

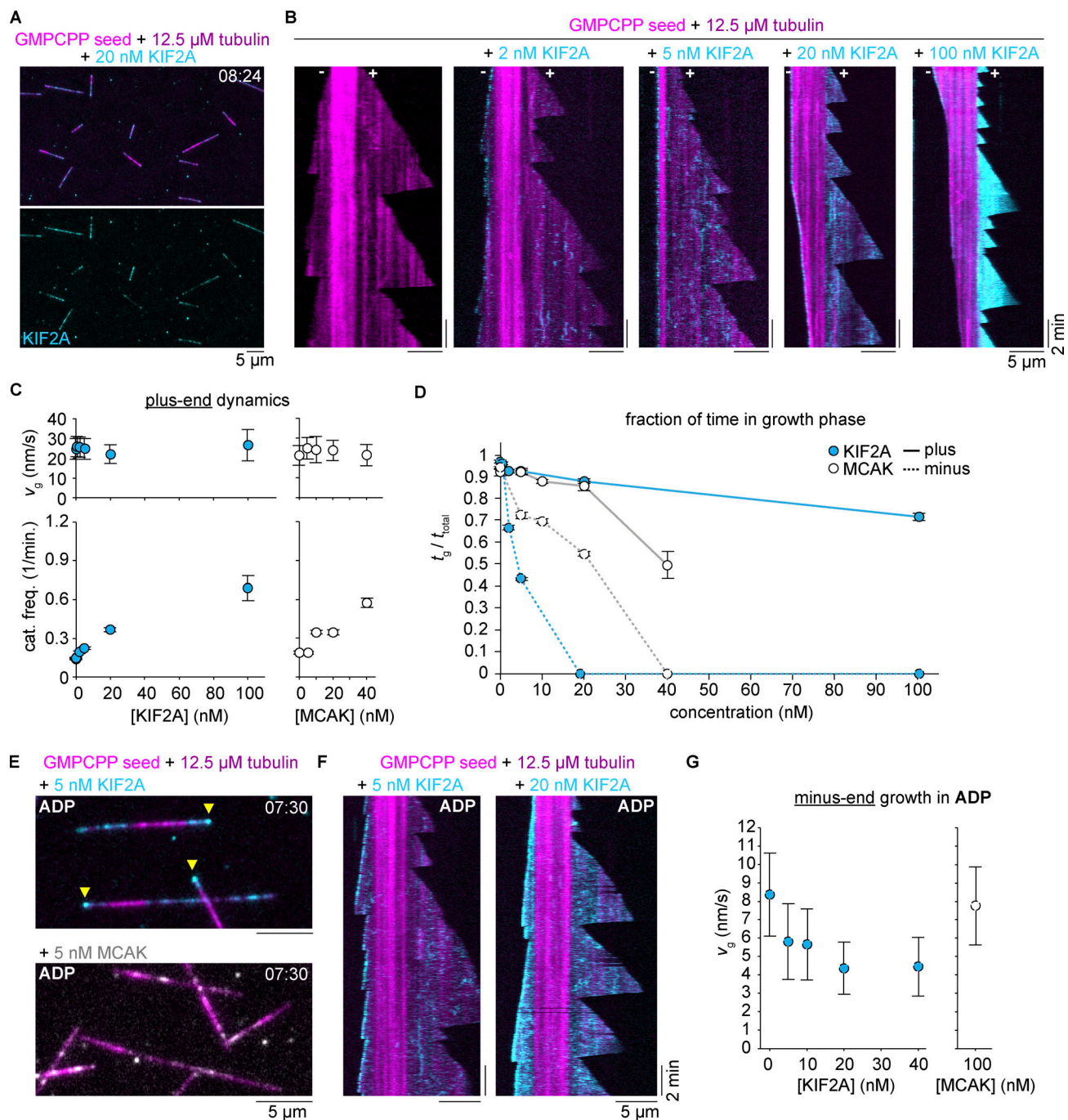


Figure 2. Preferential destabilization of dynamic microtubule minus ends by KIF2A. (A) Snapshot of dynamic microtubules polymerizing from brightly labeled GMPCPP seeds (AlexaFluor647 tubulin, magenta) in the presence of mScarlet-KIF2A (cyan). Below, mScarlet-KIF2A channel alone. (B) The sequence of kymographs for representative microtubules polymerizing from bright seeds (AlexaFluor647 tubulin, magenta) in the presence of increasing concentrations of mScarlet-KIF2A (cyan). mScarlet-KIF2A channels were additionally background subtracted and contrast was independently adjusted for each condition to show minus-end binding at a similar brightness. (C) Dynamics of microtubule plus-ends growing in the presence of increasing concentrations of mScarlet-KIF2A (left) or mCherry-MCAK (right), with a tubulin concentration of 12.5 μ M. Both proteins show no major impact on growth speed (top) and a similar increase in catastrophe rate (bottom) with increasing concentrations. Number of growth speeds measured per condition: mScarlet-KIF2A: 0 nM, $n = 502$; 0.5 nM, $n = 379$; 2 nM, $n = 508$; 5 nM, $n = 405$; 20 nM, $n = 572$; 100 nM, $n = 259$; mCherry-MCAK: 0 nM, $n = 275$; 5 nM, $n = 275$; 10 nM, $n = 406$; 20 nM, $n = 317$; 40 nM, $n = 164$. Number of catastrophe rates measured per condition: mScarlet-KIF2A: 0 nM, $n = 127$; 0.5 nM, $n = 90$; 2 nM, $n = 104$; 5 nM, $n = 71$; 20 nM, $n = 64$; 100 nM, $n = 26$; mCherry-MCAK: 0 nM, $n = 57$; 5 nM, $n = 60$; 10 nM, $n = 61$; 20 nM, $n = 41$; 40 nM, $n = 14$. Error bars are SD for growth speed and SEM for catastrophe frequency. (D) Fraction of time in the growth phase for minus and plus ends of dynamic microtubules in the presence of increasing concentrations of mScarlet-KIF2A or mCherry-MCAK and 12.5 μ M tubulin. Lines are drawn as a guide to the eye. Number of minus-end traces measured per condition: mScarlet-KIF2A: 0 nM, $n = 127$; 0.5 nM, $n = 99$; 2 nM, $n = 60$; 5 nM, $n = 63$; mCherry-MCAK: 0 nM, $n = 59$; 5 nM, $n = 21$; 10 nM, $n = 33$; 20 nM, $n = 35$. Number of plus end traces measured per condition: mScarlet-KIF2A: 0 nM, $n = 131$; 0.5 nM, $n = 93$; 2 nM, $n = 95$; 5 nM, $n = 70$; 20 nM, $n = 67$; 100 nM, $n = 32$; mCherry-MCAK: 0 nM, $n = 58$; 5 nM, $n = 65$; 10 nM, $n = 67$; 20 nM, $n = 49$; 40 nM, $n = 34$. Measurements of 0% were inferred by manual inspection of conditions in which seed ends only

depolymerized. Error bars are SEM. **(E)** Snapshot of microtubules (magenta) growing from brightly labeled seeds in the presence of mScarlet-KIF2A (top, cyan) or mCherry-MCAK (bottom, gray) in the presence of ADP and absence of ATP. Yellow arrowheads indicate mScarlet-KIF2A accumulated at the slower-growing minus ends; mCherry-MCAK did not significantly decorate either end of the growing microtubule in the presence of ADP. Images are averages of two frames taken 5 s apart. **(F)** Representative kymographs showing minus end tracking of ADP-bound mScarlet-KIF2A (cyan) and partially suppressed minus-end growth of microtubules growing from brightly labeled seeds (magenta). **(G)** Microtubule minus-end growth speeds in the presence of increasing concentrations of mScarlet-KIF2A (left) or 100 nM mCherry-MCAK (right) in ADP. Number of growth speeds measured per condition: mScarlet-KIF2A: 0, $n = 404$; 5, $n = 303$; 10, $n = 330$; 20, $n = 336$; 40, $n = 397$; mCherry-MCAK: 100, $n = 323$. Error bars are SD.

The fraction of time spent growing is a convenient single parameter to capture differences in the dynamic state of microtubule plus and minus ends. For KIF2A, it highlights a strong asymmetry between plus and minus end behavior across all KIF2A concentrations studied (Fig. 2 D). In contrast, in the presence of MCAK, we observed only a very mild asymmetry for the fraction of time plus and minus ends spent growing (Fig. 2 D). These results establish that KIF2A also has a strong minus-end preference for dynamic microtubules and allows plus ends to grow up to quite high KIF2A concentration, which is characteristically distinct from its paralog MCAK.

Having observed that KIF2A preferentially accumulates at the minus ends of stabilized microtubules in the enzymatically inactive ADP-bound state (Fig. 1, F and G), we wondered what effect ADP-bound KIF2A has on dynamic microtubule minus ends. We found that ADP-KIF2A remarkably accumulated at growing minus ends, but not at plus ends, in contrast to MCAK, which did not visibly accumulate at any dynamic end (Fig. 2, E and F). Minus-end tracking by ADP-KIF2A slowed down, but did not completely block minus-end growth (Fig. 2, F and G), an effect not observed with MCAK (Fig. 2 G). This shows that the mechanism by which KIF2A recognizes minus ends in the ADP state partially interferes with tubulin addition to the growing minus end, but that complete suppression of growth requires ATP-dependent enzymatic kinesin activity.

KIF2A drives treadmilling of dynamic microtubules

Next, we wondered what would happen at increased tubulin concentrations, where microtubules grow faster and experience fewer catastrophes. This condition would allow KIF2A to depolymerize the entire stabilized seed and then reach the minus end of the GDP lattice formed by previous plus end growth from the seed. Such a GDP minus end may represent a close mimic of a microtubule end that KIF2A interacts with inside a cell. We found that instead of inducing a stereotypical minus end catastrophe, the GDP minus end underwent relatively slow depolymerization in the presence of either untagged KIF2A or mScarlet-KIF2A (Fig. 3, A and B; and Video 3). Accumulated mScarlet-KIF2A visibly tracks the depolymerizing minus end, with occasional phases of more rapid shrinkage during which KIF2A was not accumulated (Fig. 3 B and Video 3). As the plus end continued to grow, this resulted in treadmilling of the microtubule across the glass surface, held to the surface by the crowding agent methylcellulose, until shrinkage from one or both ends completely depolymerized the microtubule or it became sufficiently small to diffuse away. This behavior is similar to a recent study reproducing microtubule treadmilling using MCAK and a combination of several other microtubule-binding proteins that increased the plus-end stability and growth speed

to counteract MCAK's destabilizing activity at plus ends (Arpağ et al., 2020). However, to our knowledge, our experiments with KIF2A are the first demonstration of treadmilling of a dynamic microtubule induced by a single microtubule-binding protein. The treadmilling activity was robust over a range of KIF2A concentrations (Fig. 3 B), and minus ends depolymerized in a KIF2A concentration-dependent manner at rates from 10 to 30 nm/s, consistent with cellular rates of poleward flux (Cameron et al., 2006; Steblyanko et al., 2020), and more than an order of magnitude slower than depolymerization episodes in the absence of KIF2A (Fig. 3 C).

γ TuRC protects microtubule minus ends from KIF2A depolymerizing activity

Next, we wondered whether KIF2A can depolymerize the minus ends of microtubules that are nucleated by γ TuRC, which typically nucleates microtubules in cells. We purified and immobilized human biotinylated and mBFP-tagged γ TuRC on a functionalized glass surface via biotin-NeutrAvidin links, and observed by TIRF microscopy γ TuRC-mediated microtubule nucleation in the presence of tubulin, as described previously (Consolati et al., 2020; Fig. 4 A). In the absence of mScarlet-KIF2A, microtubules nucleated with only the plus end growing and the minus end being tethered to an immobilized γ TuRC (Fig. 4, B and C; 0 nM KIF2A; Video 4). Notably, after nucleation microtubules remained tethered to γ TuRC throughout the entire duration of the experiment (Fig. S3 A), indicating that γ TuRC stably caps minus ends after microtubule nucleation, in agreement with previous reports (Berman et al., 2023; Consolati et al., 2020; Rai et al., 2022 Preprint; Thawani et al., 2020; Wicczorek et al., 2021).

Next, we added mScarlet-KIF2A at different concentrations to the γ TuRC nucleation assay. Microtubules still nucleated from γ TuRC, but nucleation became less efficient at higher KIF2A concentrations (Fig. 4 B and Video 4). Quantifying the number of nucleated microtubules over time revealed that the nucleation rate (slopes in Fig. 4 D) decreased with increasing concentrations of mScarlet-KIF2A but to a considerably lesser extent than with mCherry-MCAK (Fig. 4 E), which was reported previously to inhibit γ TuRC-mediated microtubule nucleation (Thawani et al., 2020). As observed for microtubules grown from GMPCPP-seeds (Fig. 2 C), KIF2A at higher concentrations increased the catastrophe frequency of the plus ends of γ TuRC-nucleated microtubules (Fig. 4, C and F) without affecting their growth speed (Fig. 4 G). These results indicate that plus-end destabilization of the nascent microtubule nucleus forming on γ TuRC negatively influences microtubule nucleation. Nevertheless, γ TuRC-mediated nucleation tolerates much higher concentrations of KIF2A than MCAK, likely due to KIF2A's end selectivity.

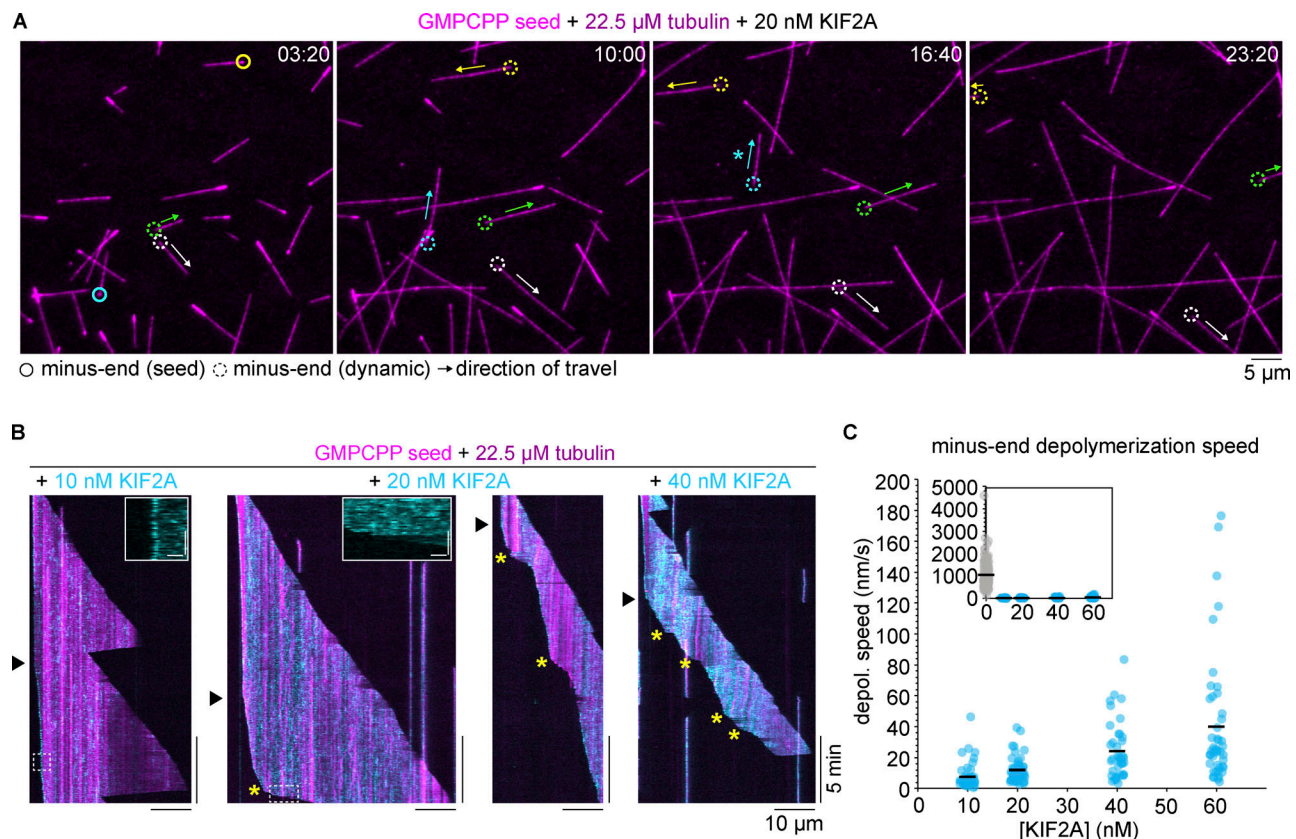


Figure 3. Treadmilling of dynamic microtubules driven by KIF2A. (A) Time sequence snapshots of microtubules growing from brightly labeled seeds (magenta, Atto647) in the presence of 20 nM untagged KIF2A. Circles track the depolymerizing minus ends of selected microtubules that undergo treadmilling. A solid circle indicates the microtubule is still attached to the brightly labeled GMPCPP seed, whereas a dashed circle indicates the seed has completely depolymerized and the microtubule (including the minus end) is composed of only GTP/GDP tubulin. For better distinction and identification of the selected microtubules, both solid and dashed circles are color coded. Arrows indicate the direction of “travel” across the glass surface. The asterisk indicates that the microtubule was lost from view after this timepoint following a plus-end catastrophe. **(B)** Representative kymographs of microtubules (magenta) that are released from the stabilized GMPCPP seed after depolymerization by mScarlet-KIF2A (cyan), indicated by the black arrowhead. Minus-end depolymerization was heterogeneous: asterisks indicate instances of increased depolymerization speed. Insets: Enlarged regions of kymographs showing mScarlet-KIF2A localization at minus ends undergoing periods of “slow” (10 nM KIF2A inset) and “fast” (20 nM KIF2A inset) depolymerization. Inset scale bars: horizontal, 1 μ m; vertical, 30 s. **(C)** Average depolymerization rates of minus ends of treadmilling microtubules, measured from microtubules that are no longer attached to seeds, in the presence of various concentrations of mScarlet-KIF2A. Each measurement is plotted as a semi-transparent dot (with random x-jitter to improve visualization) and the mean is overlaid as a black bar. Inset: The same data with a 0 nM KIF2A timepoint included (where each measurement is made from each instance of depolymerization after catastrophe) and an extended y axis. Number of depolymerization speeds measured per condition: mScarlet-KIF2A: 0 nM, $n = 264$; 10 nM, $n = 74$; 20 nM, $n = 76$; 40 nM, $n = 62$; 60 nM, $n = 68$.

Remarkably, the large majority of the inherently more KIF2A-sensitive microtubule minus ends were now completely protected from the depolymerizing activity of KIF2A by the γ TuRC cap (Fig. 4 C). Despite the presence of KIF2A, almost all microtubule minus ends remained protected by γ TuRC for the entire duration of the experiment, as demonstrated by their minus ends remaining tethered to the functionalized glass surface (Fig. 4, C and H). This is in contrast to uncapped minus ends of dynamic microtubules (Figs. 2 and 3) or of occasionally spontaneously nucleated microtubules in the γ TuRC-nucleation assay (Fig. S3 B), where the minus ends are depolymerized by KIF2A (Fig. 4 I). Nevertheless, we still sporadically observed microtubules detaching from γ TuRC in the presence of KIF2A (mScarlet-KIF2A: Fig. 4 H; untagged KIF2A: Fig. S3 C). These microtubules first nucleated from γ TuRC and remained minus-end capped for a period of time

until KIF2A apparently destabilized the connection with the γ TuRC and drove slow minus-end depolymerization (Fig. 4 J and Video 5). This was accompanied by minus end accumulation of KIF2A and resulted in treadmilling of the majority of γ TuRC-released microtubules (Fig. 4 J and Video 5), as observed for seed-grown microtubules (Fig. 3 B). In the absence of KIF2A or in the presence of mCherry-MCAK, we did not observe a single released microtubule (Fig. 4 H and Fig. S3 C), demonstrating that although microtubule release from γ TuRC is a rare event, it can be selectively triggered by KIF2A.

Together KIF2A and spastin uncapped γ TuRC-nucleated microtubules allowing microtubule treadmilling

This raised the question of whether microtubule severases that have been reported to promote poleward microtubule flux in the spindle during mitosis (Guerreiro et al., 2021; Huang et al., 2021;

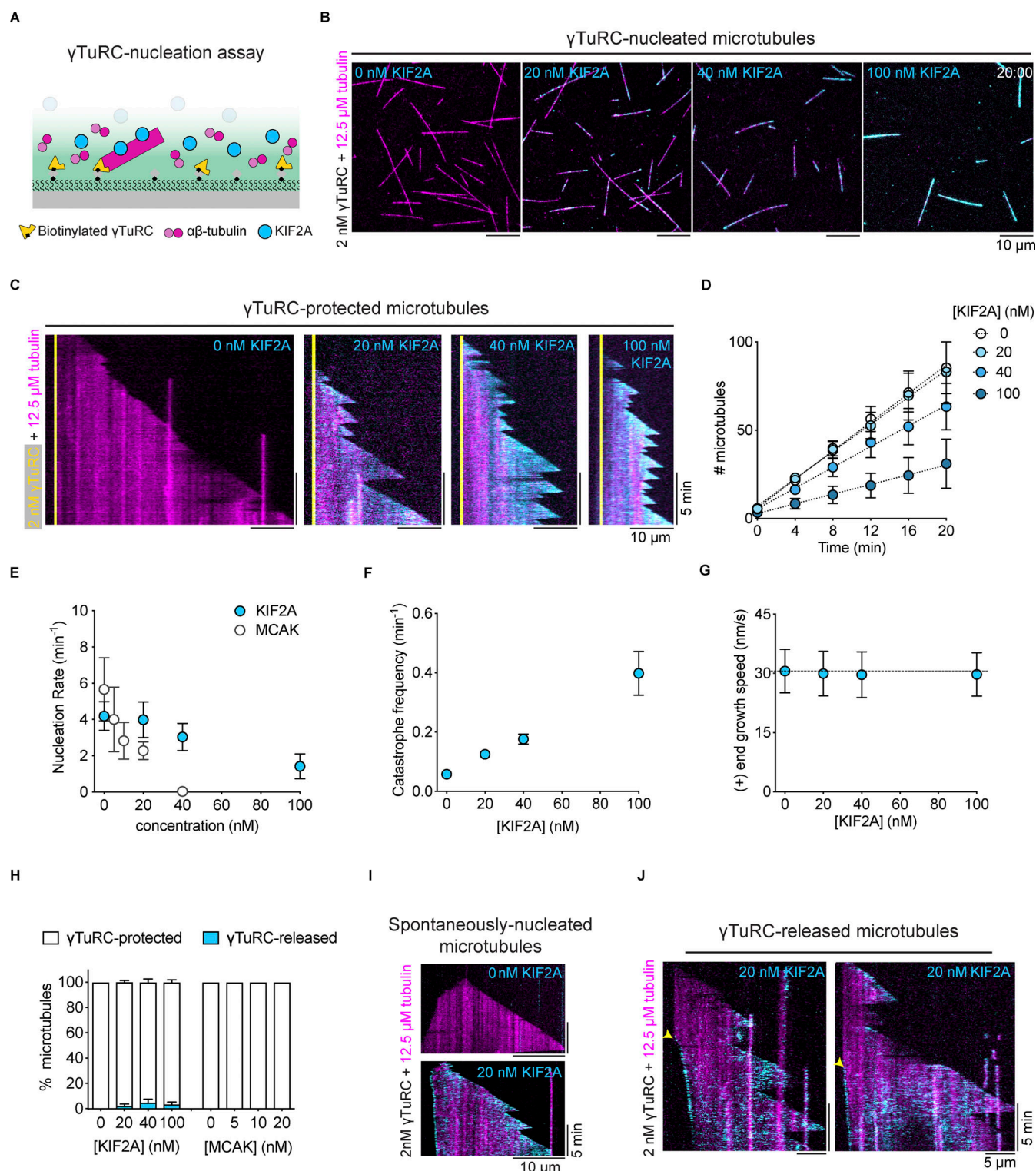


Figure 4. γ TuRC-nucleated microtubules are protected from KIF2A depolymerizing activity. (A) Schematic of the TIRF microscopy-based γ TuRC-nucleation assay. Biotinylated and mBFP-tagged γ TuRC is immobilized on a biotin-PEG-functionalized glass surface via NeutrAvidin, followed by the addition of tubulin and KIF2A. (B) TIRF microscopy images of γ TuRC-nucleated microtubules in the absence (left) and presence of mScarlet-KIF2A (cyan), 20 min after the start of imaging. Surface-immobilized γ TuRC is not shown. (C) Representative kymographs of microtubules nucleating from γ TuRC (yellow) for the conditions shown in B. (D–G) Numbers of microtubules nucleated over time (D), microtubule nucleation rates for mScarlet-KIF2A and mCherry-MCAK (E), catastrophe frequencies (F), and microtubule plus-end growth speeds (G) for the conditions in B. Circles represent mean values and error bars are SEM (D–F) and SD (G). For symbols without visible error bars, error bars are smaller than the symbol size. The lines in D represent linear regressions. The dashed line in G represents the mean microtubule plus-end growth speeds in the absence of mScarlet-KIF2A. Nucleation rates (E) were calculated from the slope of the linear regression (mScarlet-KIF2A: D; mCherry-MCAK: not shown). Number of

microtubules analyzed for the catastrophe frequency (F) per mScarlet-KIF2A concentration: 0 nM, $n = 191$; 20 nM, $n = 186$; 40 nM, $n = 122$; 100 nM, $n = 65$; number of microtubule growth speeds (G) measured per mScarlet-KIF2A concentration: 0 nM, $n = 187$; 20 nM, $n = 169$; 40 nM, $n = 79$; 100 nM, $n = 66$. Data for plots was pooled from three independent experiments. (H) Percentage of microtubules that either remain protected by γ TuRC or are released after nucleation, for the indicated concentrations of mScarlet-KIF2A and mCherry-MCAK. Number of microtubules analyzed per condition: mScarlet-KIF2A–0 nM, $n = 256$; 20 nM, $n = 249$; 40 nM, $n = 190$; 100 nM, $n = 91$; mCherry-MCAK–0 nM, $n = 332$; 5 nM, $n = 281$; 10 nM, $n = 182$; 20 nM, $n = 156$. Data was pooled from three independent experiments. Error bars shown for mScarlet-KIF2A concentrations are SEM. (I) Representative kymographs of occasionally observed spontaneously nucleated microtubules, recognized by growth at both ends after nucleation, in a γ TuRC nucleation assay, in the absence (top image) or presence (bottom image) of 20 nM of mScarlet-KIF2A (cyan). (J) Representative kymographs of γ TuRC-nucleated microtubules that are released after nucleation in the presence of 20 nM of mScarlet-KIF2A (cyan). Yellow arrowheads indicate the moment of γ TuRC-uncapping and the beginning of accumulation of mScarlet-KIF2A at the released and slowly depolymerizing microtubule minus end. 2 nM γ TuRC was used for initial surface immobilization in all experiments.

Zhang et al., 2007) can promote the generation of uncapped microtubules and therefore KIF2A-accessible minus ends of γ TuRC-nucleated microtubules. To be able to test this, we purified human spastin and fluorescently labeled mGFP-spastin (Fig. S1, F and G) and verified their microtubule severing activity by adding them to glass-surface immobilized GMPCPP-stabilized microtubules. Although mGFP-spastin was a little less efficient than the unlabeled severase, both caused microtubule disintegration within minutes (Fig. S4, A and B, top panel), as it was observed for related severases (McNally et al., 1996; Roll-Mecak and Vale, 2005; Vemu et al., 2018). However, the vast majority of γ TuRC-nucleated microtubules did not show any severing events in the presence of spastin ($\sim 99\%$, Fig. 5 A). This agrees with previous reports of microtubule severing being inefficient in the presence of free tubulin (Bailey et al., 2015; Jiang et al., 2017; Kuo et al., 2019; Vemu et al., 2018).

When we added mGFP-spastin and mScarlet-KIF2A in combination with stabilized microtubules, they were now severed considerably faster than in the presence of spastin alone (Fig. S4 B, bottom panel). Measuring the fluorescence intensity along the initial microtubule contour over time revealed that when only GFP-spastin was present, its binding initially increased as the microtubule started to become severed and then decreased as the microtubule disappeared (Fig. S4 C). In the additional presence of KIF2A, this process exhibited a similar pattern but at an accelerated rate (Fig. S4 C), suggesting that KIF2A supports severing by spastin and that both act in synergy. Indeed, KIF2A's fluorescence intensity peaked right after the peak of the mGFP-spastin intensity (Fig. S4 C).

When we added both spastin and KIF2A to the γ TuRC nucleation assay, we also observed an increased number of severing events along the lattice of γ TuRC-nucleated microtubules compared with spastin being present alone (yellow asterisks, Fig. 5 B i and ii; severing observed in $\sim 7\%$ of microtubules). After severing, the newly formed plus ends displayed dynamic instability behavior, switching between growth and fast shrinkage episodes (Fig. 5 B and Video 6), whereas the newly formed minus ends were slowly depolymerized by KIF2A (Fig. 5 B), resulting in treadmilling of the newly generated free microtubule (Fig. 5 B ii). Remarkably, in the combined presence of mScarlet-KIF2A and spastin, we observed also substantially more frequent detachments of microtubules from surface-tethered γ TuRC, also causing them to treadmill (Fig. 5 C and Video 7). Microtubule release from immobilized γ TuRC increased from $\sim 1\%$ and $\sim 2\%$ in the presence of spastin or KIF2A alone, respectively, to almost 40% when spastin and KIF2A were both present (Fig. 5 D). This

release, induced by severing at or near the γ TuRC/microtubule interface, is approximately five times higher than the percentage of microtubules severed at any other point along the lattice (Fig. 5 E), despite the much larger number of potential severing sites along the entire microtubule length compared with the single γ TuRC cap at the minus end. Because we did not observe mGFP-spastin directly binding to surface-immobilized γ TuRC (Fig. S4 D), we conclude that the γ TuRC/microtubule interface is orders of magnitudes more sensitive to the combined action of KIF2A and spastin than an average microtubule lattice site, favoring γ TuRC uncapping over lattice severing. Taken together, our results demonstrate that spastin and KIF2A act in synergy to trigger microtubule minus-end release from γ TuRC and subsequent treadmilling, consistent with the proposed function of KIF2A and severases at spindle poles.

Discussion

We discovered here that the kinesin-13 KIF2A is a microtubule minus-end depolymerase that can induce flux-like microtubule treadmilling. Although KIF2A acts mildly on plus ends, it has a strong preference for minus-end destabilization, establishing it as an asymmetric microtubule depolymerase. This property distinguishes KIF2A from its paralog MCAK which destabilizes both microtubule ends similarly. Moreover, we found that the presence of a γ TuRC cap at minus ends inhibits minus-end depolymerization by both depolymerases. To induce treadmilling of γ TuRC-nucleated microtubules, active uncapping of minus ends is required, which can be achieved by the combined activities of KIF2A and the severase spastin. Taken together, we show here that a γ TuRC/KIF2A/severase module can provide the activities required for both microtubule nucleation and controlled microtubule minus-end depolymerization at spindle poles, in agreement with the requirements for the generation of microtubule flux in mitotic and meiotic spindles.

Minus-end recognition by KIF2A appears to be different from the generic microtubule end recognition mechanism of kinesin-13s, in which the motor domain in its ATP state binds to and stabilizes a curved microtubule protofilament (Asenjo et al., 2013; Benoit et al., 2018; Trofimova et al., 2018; Wang et al., 2017). We found that KIF2A binds preferentially to minus ends also in the presence of ADP, showing that enzymatic activity is not required for minus end recognition. Because ADP-KIF2A also slows down microtubule growth and because minus-end capping by iE5 and γ TuRC prevents KIF2A minus-end accumulation, it is tempting to speculate that KIF2A's minus-end recognition

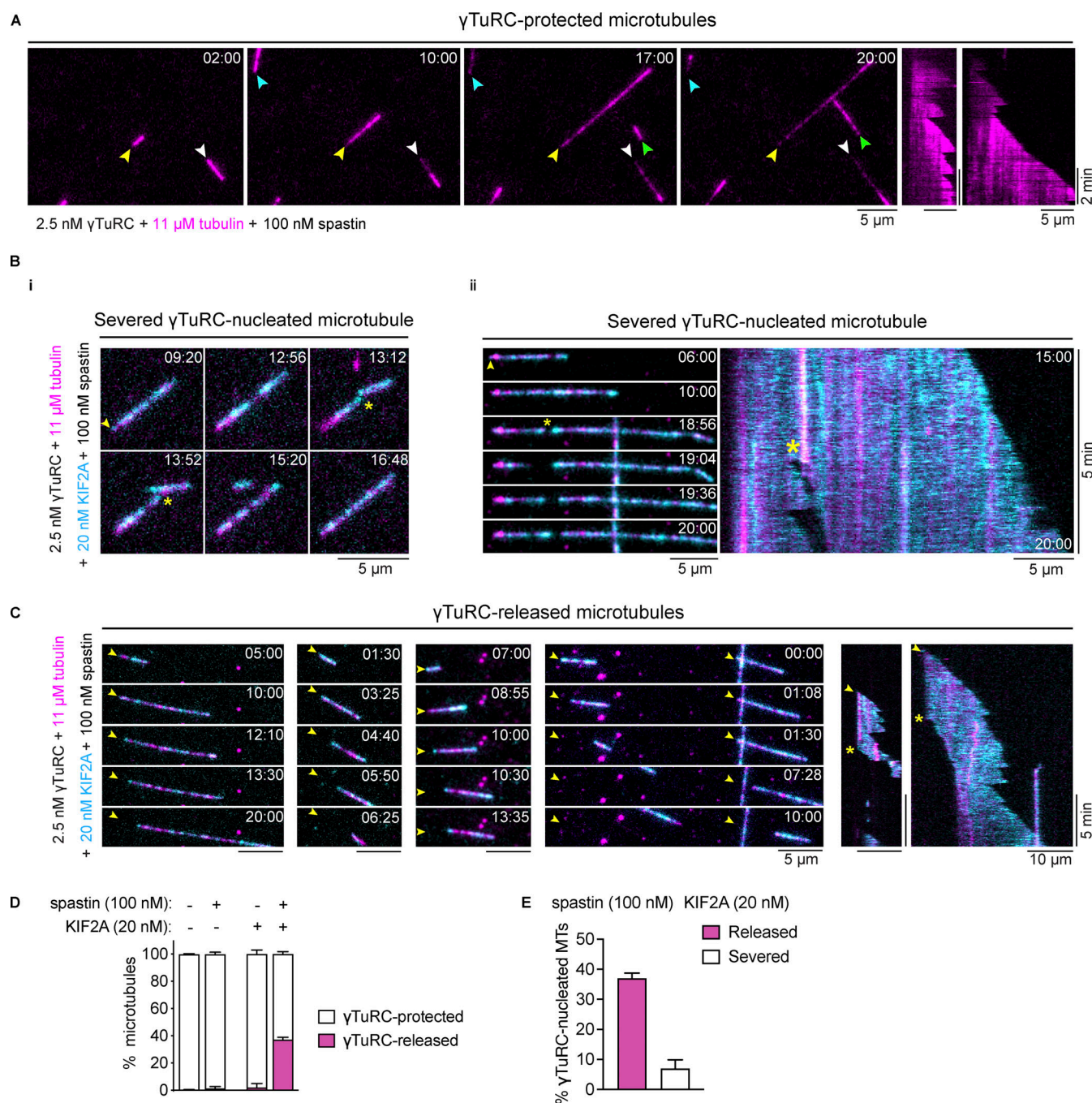


Figure 5. γ TuRC-nucleated microtubules are uncapped by KIF2A and spastin allowing microtubule treadmilling. (A) Time sequence of TIRF microscopy images and kymographs of microtubules (magenta) nucleated by surface-immobilized γ TuRC in the presence of 11 μ M Cy5-tubulin (5.4% labeling percentage), which remain unaffected by 100 nM of spastin. Arrowheads point to γ TuRC-capped microtubule minus ends. (B) Time sequence of TIRF microscopy images and kymograph of γ TuRC-nucleated microtubules (magenta) that were severed in the presence of 11 μ M Cy5-tubulin, 20 nM mScarlet-KIF2A (cyan), and 100 nM of spastin. Yellow arrowheads and asterisks indicate γ TuRC-capped microtubule minus-ends and severing events, respectively. (C) Time sequence of TIRF microscopy images and kymographs of γ TuRC-nucleated microtubules (magenta) that were released from γ TuRC by the combined action of mScarlet-KIF2A (cyan) and spastin. Conditions as in B. Yellow arrowheads point to the γ TuRC-nucleation sites of microtubules and yellow asterisks indicate the release of the microtubules from γ TuRC, leaving the minus end uncapped for depolymerization by mScarlet-KIF2A (cyan). (D) Percentage of microtubules that either remain protected by γ TuRC or are released after nucleation for the indicated concentrations of mScarlet-KIF2A and spastin. Number of microtubules analyzed per condition: mScarlet-KIF2A and spastin: 0 nM, $n = 228$; mScarlet-KIF2A 0 nM and spastin 100 nM, $n = 152$; mScarlet-KIF2A 20 nM and spastin 0 nM, $n = 160$; mScarlet-KIF2A 20 nM and spastin 100 nM, $n = 222$. Data for plots were pooled from at least two independent experiments. Error bars are SEM. (E) Percentage of released and severed γ TuRC-nucleated microtubules for the indicated concentration of spastin and mScarlet-KIF2A. Number of microtubules analyzed per condition: mScarlet-KIF2A 20 nM and spastin 100 nM, $n = 222$. Error bars are SEM. In all experiments, 2.5 nM γ TuRC was used for surface immobilization. The time stamps indicate min:s.

may involve binding to at least part of the exposed α -tubulin at microtubule minus ends. In the future, biochemical and structural studies will be required to identify the mechanism underlying KIF2A's remarkable minus-end binding preference.

In interphase cells, individual microtubules have been observed to adopt a treadmilling state in which net plus-end growth is balanced by net minus-end depolymerization, which has been associated with loss of minus-end stabilizers (Goodwin and Vale, 2010; Rodionov and Borisy, 1997; Shaw et al., 2003; Waterman-Storer and Salmon, 1997). Remarkably, the kinesin-13 KLP10A, which in mitosis seems to share some functional homology with KIF2A (Laycock et al., 2006; Rath et al., 2009; Rogers et al., 2004), was observed to localize to shrinking minus ends and to induce treadmilling of microtubules in *Drosophila* cells when the minus-end stabilizing protein patronin was knocked down (Goodwin and Vale, 2010).

Early in vitro work with purified proteins investigated the possibility of treadmilling being an intrinsic property of microtubules, but later it became clear that the intrinsic dynamic behavior of microtubules is dominated by dynamic instability at both ends (Grego et al., 2001; Margolis and Wilson, 1978; Mitchison and Kirschner, 1984). We find here that purified KIF2A can trigger microtubule treadmilling in vitro, resulting as the consequence of the combination of two of its properties. First, it destabilizes minus ends more strongly than plus ends, so that in a certain concentration regime, plus ends grow dynamically whereas minus ends shrink; and second, in contrast to the intrinsically fast depolymerization after typical catastrophe events, KIF2A induces mainly slow minus-end depolymerization, while remaining end accumulated at the shrinking minus ends, which can then be balanced by (net) plus-end growth. The mechanism of this slow-down of minus-end depolymerization is unknown but might be related to the formation of higher-order structures formed by curved, depolymerizing protofilaments and KIF2A, as observed in electron microscopy with different members of the kinesin-13 family (Moores et al., 2006; Tan et al., 2006, 2008; Zhang et al., 2013).

A recent study reported the in vitro reconstitution of microtubule treadmilling with a combination of several vertebrate microtubule-binding proteins (Arpağ et al., 2020), evidence of which can also be seen in earlier in vitro work with the corresponding *Drosophila* orthologs (Moriwaki and Goshima, 2016). Because the symmetric depolymerase MCAK was used in this recent work, additional activities were required to generate an asymmetry in the control of microtubule dynamics. This was achieved by including the plus-end specific microtubule polymerase XMAP215 and the anti-catastrophe factor CLASP2, resulting in microtubule treadmilling with growing plus ends and shrinking minus ends. These additional factors were not required in our reconstitution due to the inherently asymmetric activity of KIF2A with respect to the two microtubule ends, simplifying the minimal requirements for microtubule treadmilling. In cells, KIF2A's intrinsic minus-end preference can be enhanced by proteins that promote its minus-end accumulation (Guan et al., 2023).

Our study revealed that γ TuRC and kinesin-13s compete in two different ways. First, we showed that microtubule

nucleation by γ TuRC is inhibited in a dose-dependent manner by both KIF2A and MCAK, however, to a much lesser extent by KIF2A. This suggests that kinesin-13 depolymerase activity destabilizes nascent microtubule plus-ends beginning to grow on a γ TuRC template and that this destabilization is weaker for KIF2A due to its end selectivity. Second, once the microtubule has nucleated, γ TuRC caps the minus end and now inhibits minus-end depolymerization by kinesin-13s, an activity reminiscent of the minus-end binding protein patronin/CAMSAP that however binds minus ends very differently from γ TuRC (Atherton et al., 2017; Goodwin and Vale, 2010).

Our finding that spastin and KIF2A in combination, but not alone, can efficiently induce microtubule severing in the presence of free tubulin, thereby leading to KIF2A-mediated minus-end depolymerization, has several interesting implications. First, severase-induced lattice damage appears to provide an entry point for KIF2A to promote lattice destabilization and/or interfere with lattice repair by soluble tubulin (Schaedel et al., 2015; Vemu et al., 2018), thereby promoting complete severing. KIF2A's severase-supporting effect may explain why in cytoplasmic extract severases appear much more active than purified severases in the presence of free tubulin in vitro (Vale, 1991; Vemu et al., 2018). α -Tubulins likely become exposed when spastin removes tubulins from the lattice where KIF2A might be able to act and increase the size of the damage site. Our results also highlight that severase activity in the presence of free tubulin can be promoted by mechanisms beyond the physical recruitment of severases to the microtubule, as shown for ASPM and katanin (Jiang et al., 2017).

Moreover, we observed that also γ TuRC uncapping was promoted by the combined action of KIF2A and spastin, and remarkably was more frequent than microtubule severing, although (1) γ TuRC prevents microtubule minus-end binding of KIF2A, (2) γ TuRC and spastin do not directly interact, and (3) many more potential severing sites exist along the microtubule lattice than at the γ TuRC/microtubule minus end interface. This implies that the γ TuRC/minus end connection is much more sensitive to the combined action of spastin and KIF2A than the rest of the microtubule lattice. Although the γ TuRC cap at minus ends is very stable in the absence of other proteins, it appears to become a structurally weak point in the presence of KIF2A and a severase, allowing preferential active minus-end uncapping, possibly not only to enable microtubule treadmilling but also to recycle γ TuRC for new rounds of microtubule nucleation. γ TuRC-uncapping by KIF2A and spastin is functionally distinct from recently reported uncapping by CAMSAPs that remove γ TuRC by inducing slow minus-end polymerization, which is possibly more adapted to the function of microtubules in neurons (Rai et al., 2022 Preprint).

In conclusion, we characterized in vitro a minimal protein module that can be found at the poles of mitotic and meiotic spindles during cell division and that can control apparently antagonistic activities at this location. On one hand, microtubules need to be nucleated, which results in the stable capping of their minus ends by γ TuRC. On the other hand, minus ends also need to be uncapped and slowly shrink for microtubule flux in the spindle to occur. γ TuRC, KIF2A, and a severase in

combination can provide this control of microtubule minus-end dynamics as required at spindle poles. A major element of this control is the asymmetric action of the kinesin-13 KIF2A, adding to the list of other plus or minus-end selective microtubule-associated proteins that control the functionally important asymmetric dynamic properties of the two microtubule ends in cells.

Materials and methods

Protein constructs and cloning

Human KIF2A (NCBI reference sequence: NP_004511.2; codon-optimized for insect cell expression by GeneArt) and MCAK (NCBI reference sequence: NP_006836.2) constructs were cloned similarly to previously published constructs (Roostalu et al., 2018). Briefly, coding sequences were amplified by PCR and cloned into a pFastBac expression vector for expression in Sf9 or Sf21 cells (Thermo Fisher Scientific), including a StrepTagII-coding sequence at the N-terminal of the construct, to generate the following constructs: StrepTagII-KIF2A, StrepTagII-mScarlet-G₆S-KIF2A, and StrepTagII-mCherry-G₅A-MCAK. Constructs included a region coding for a TEV protease recognition site between the StrepTagII sequence and the desired construct for cleavage of the tag. The monomeric red fluorescent protein variants mScarlet (Bindels et al., 2017) and mCherry (Shaner et al., 2004) were separated from the N-terminus of KIF2A and MCAK by flexible linker regions. The sequence coding for MCAK included an extra isoleucine residue after the initial methionine as a consequence of the cloning process.

The human spastin and mGFP-spastin constructs were cloned using the sequence corresponding to isoform 3 (UniProtKB reference sequence Q9UBP0-3; OriGene), a shortened variant derived from the use of an alternative start residue (Met-87), as identified and used in previous works (Claudiani et al., 2005; Roll-Mecak and Vale, 2005). The spastin sequence was amplified by PCR and cloned into a pETMZ and a pETMZ-mGFP vector for expression in *Escherichia coli*, generating the constructs His₆-Ztag-TEV-spastin and His₆-Ztag-TEV-mGFP-spastin. The sequence coding for spastin included an extra isoleucine residue after the initial methionine as a consequence of the cloning process.

The plasmids for bacterial expression of the αRep iE5 and the tandem repeat Design-Ankirin-Repeat-Protein (DARPin)—(D1)₂—are described elsewhere (Campanacci et al., 2019; Pecqueur et al., 2012).

Protein expression and purification

Tubulin was prepared from pig brains as previously described (Castoldi and Popov, 2003). Tubulin was further purified by recycling and some tubulin was labeled with AlexaFluor647-N-hydroxysuccinimide ester (NHS; Sigma-Aldrich), Atto647-NHS (Sigma-Aldrich), Cy5-NHS (Lumiprobe), or biotin-NHS (Thermo Fisher Scientific), as described (Consolati et al., 2022). Final concentrations and fluorescent labeling ratios were determined by UV absorption using NanoDrop One/OneC (Thermo Fisher Scientific; extinction coefficient for tubulin, 115,000 M⁻¹ cm⁻¹;

molecular weight, 110 kD) after final ultracentrifugation, before aliquoting and snap-freezing. Aliquoted tubulin was then placed in liquid nitrogen.

KIF2A, mScarlet-KIF2A, and mCherry-MCAK constructs were expressed using Sf21 cells (Thermo Fisher Scientific) according to the manufacturer's protocols. Cell pellets from 500 ml of culture were snap-frozen and stored at -80°C. Thawed pellets of cells expressing KIF2A and mCherry-MCAK constructs were resuspended in ice-cold KIF2A lysis buffer (50 mM Na-phosphate, 300 mM KCl, 1 mM MgCl₂, 1 mM ethylene glycol bis(2-aminoethyl ether)tetraacetic acid [EGTA], 5 mM β-mercaptoethanol [β-ME], and 0.5 mM adenosine triphosphate [ATP], pH 7.5), supplemented with DNaseI (Sigma-Aldrich) and protease inhibitors (cOmplete EDTA-free; Roche). The lysate was homogenized in a glass douncer on ice (40 strokes) and subsequently clarified by centrifugation at 50,000 rpm in a Ti70 rotor (Beckman Coulter) at 4°C for 45 min. The supernatant was then run over a 5 ml StrepTrap HP or XT column (Cytiva) at 0.5 ml min⁻¹ using a peristaltic pump at 4°C. Bound protein was washed with 10 ml of KIF2A lysis buffer supplemented with ATP to a total of 5 mM at 0.5 ml min⁻¹ and then eluted in 0.5 ml fractions using KIF2A lysis buffer supplemented with 2.5 mM d-desthiobiotin (for StrepTrap HP) or 50 mM biotin (for StrepTrap XT). Protein-containing fractions were collected, pooled, supplemented with protease inhibitors, and cleaved with TEV protease overnight on ice. The buffer was then exchanged to KIF2A gel filtration buffer (lysis buffer with 0.1 mM ATP instead of 0.5 mM) using HiPrep 26/10 or PD10 desalting columns (Cytiva) to remove the d-desthiobiotin/biotin, and the protein was run over the StrepTrap column again at 0.5 ml min⁻¹ and 4°C to obtain only cleaved protein. The cleaved protein was then concentrated (Vivaspin 30,000 MWCO; Sartorius) and ultracentrifuged in a TLA-120.2 rotor (Beckman Coulter) at 80,000 rpm for 10 min at 4°C before further purification by gel filtration using a HiLoad 16/600 Superose 6 prep grade column (Cytiva), equilibrated in KIF2A gel filtration buffer. The protein that eluted as a single peak was collected and concentrated to 3–5 mg ml⁻¹, ultracentrifuged in a TLA 120.2 rotor (Beckman Coulter) at 80,000 rpm for 15 min at 4°C, snap-frozen, and stored in liquid nitrogen. mCherry-MCAK was supplemented with 10% sucrose (wt/vol) before the final ultracentrifugation.

mScarlet-KIF2A was purified similarly to KIF2A and mCherry-MCAK, with the following modifications: the lysate was homogenized using the EmulsiFlex-C5 (10,000–15,000 psi; Avestin). Affinity chromatography was performed using the Äkta Pure System (Cytiva) instead of the peristaltic pump and gel filtration using a HiLoad 16/600 Superdex 200 pg column (Cytiva). mScarlet-KIF2A was also supplemented with 10% sucrose (wt/vol) before the final ultracentrifugation.

His₆-Ztag-spastin was expressed in BL21 pRIL *E. coli* cultures at 18°C overnight, pellets of which were snap-frozen and stored at -80°C. For purification, pellets were resuspended in spastin lysis buffer (50 mM 4-(2-hydroxyethyl)-1-piperazineethanesulfonic acid [HEPES], 300 mM KCl, 5 mM MgCl₂, 25 mM sucrose, 0.5 mM ATP, and 1 mM β-ME, pH 8.0) supplemented with DNase I and protease inhibitors. Cells were lysed using a microfluidizer and cleared by centrifugation. Cleared lysate was loaded onto a HiTrap

column loaded with cobalt (Cytiva) and washed with spastin wash buffer (50 mM HEPES, 300 mM KCl, 2 mM MgCl_2 , 1 mM β -ME, 50 mM arginine, 50 mM glutamate, 25 mM sucrose, 0.1 mM ATP, and 20 mM imidazole, pH 7.5) before eluting with spastin wash buffer supplemented with imidazole to a total of 400 mM. Eluted protein fractions were pooled and the buffer was exchanged with spastin wash buffer using PD-10 columns and cleaved with TEV protease overnight. Uncleaved protein and cleaved His₆-Ztag domains were separated from cleaved protein by incubation with TALON resin (Clontech). The supernatant was buffer exchanged to MES A buffer (20 mM MES, 100 mM KCl, 2 mM MgCl_2 , 0.1 mM ATP, and 5 mM β -ME, pH 6.0) using PD-10 columns. The buffer-exchanged protein was ultracentrifuged and bound to a Mono S 5/50 G ion exchange column equilibrated in MES A. Protein was eluted from the column with a gradient of MES B buffer (20 mM MES, 1,000 mM KCl, 2 mM MgCl_2 , 0.1 mM ATP, and 5 mM β -ME, pH 6.0; 3% ml^{-1} gradient). Eluted protein was then gel-filtered using a HiLoad 16/600 Superdex 200 pg column (Cytiva) equilibrated with spastin gel-filtration buffer (50 mM HEPES, 300 mM KCl, 0.1 mM ATP, 2 mM MgCl_2 , 5 mM β -ME, 50 mM arginine, 50 mM glutamate, and 250 mM sucrose, pH 7.5). Pooled fractions were then concentrated, ultracentrifuged, aliquoted and snap-frozen, and stored in liquid nitrogen. Before use in experiments, frozen aliquots were thawed and dialyzed against KIF2A gel-filtration buffer (Slide-A-Lyzer MINI; Thermo Fisher Scientific). Dialyzed protein was then concentrated, ultracentrifuged in a TLA 120.2 rotor at 80,000 rpm for 10 min at 4°C, snap-frozen, and stored in liquid nitrogen.

His₆-Ztag-mGFP-spastin was expressed and purified using the same procedure as for human spastin.

KIF2A, mScarlet-KIF2A, mCherry-MCAK, and spastin concentrations were all measured by Bradford assay (Bio-Rad) against a bovine serum albumin standard (Pierce/Thermo Fisher Scientific) using snap-frozen and thawed protein aliquots. Reported concentrations refer to monomers based on their predicted molecular weights.

Biotinylated γ TuRC-mBFP-AviTag was purified from HeLa-Kyoto cells stably expressing GCP2-mBFP-AviTag and the biotin ligase HA-BirA, essentially as previously described (Consolati et al., 2020). γ TuRC-mBFP-AviTag concentration was estimated by UV absorption using NanoDrop One/OneC (Thermo Fisher Scientific; molecular weight: 2.2 MD), yielding 0.4–0.8 mg from 60 g of HeLa-Kyoto cells.

The α Rep iE5 was expressed and purified as described elsewhere (Campanacci et al., 2019).

The DARPin (D1)₂ (Pecqueur et al., 2012) was expressed in *E. coli* BL21-CodonPlus (DE3)-RIL cells grown in an LB medium. When reaching an OD₆₀₀ of 0.6 at 37°C, the expression of (D1)₂ was induced with 0.5 mM isopropyl β -D-1-thiogalactopyranoside (IPTG) for 20 h at 18°C. Cells from 500 ml expressing cultures were harvested by centrifugation (9,000 $\times g$ for 10 min, at 4°C) and cell pellets were stored at –80°C. (D1)₂ was purified as previously described (Pecqueur et al., 2012), with some modifications. Briefly, cells were resuspended in lysis buffer (50 mM Tris, pH 8, 1 mM MgCl_2 , and 10 mM imidazole; 10 ml per gram of

pellet) and supplemented with 0.3 mg ml^{-1} lysozyme, 0.25 units ml^{-1} of benzonase and protease inhibitor mix (cOmplete EDTA free, Roche). Cells were lysed using the EmulsiFlex-C5 (15,000 psi; Avestin) and the lysate was clarified by centrifugation at 20,000 $\times g$ for 40 min at 4°C. The supernatant was loaded using a peristaltic pump in 1 ml (bed volume) of Ni-NTA agarose (QIAGEN) packed in a Poly-Prep Chromatography Column (Cat #731-1550; Bio-Rad). Bound protein was washed with 30 ml of wash buffer (20 mM K-phosphate, pH 7.2, 1 mM MgCl_2 , 0.5 mM EGTA, 100 mM KCl, 1 mM ATP, 10 mM imidazole, and 5 mM DTT), followed by elution in wash buffer without ATP and with 100 mM imidazole instead of 10 mM. Eluted protein was subjected to size exclusion chromatography on a HiLoad 16/600 Superdex 200 pg column (Cytiva) equilibrated with wash buffer without ATP and imidazole. Protein-containing fractions were pooled, concentrated using an Amicon centrifugal unit (MWCO 10,000; Millipore), and ultracentrifuged in a TLA110 rotor (Beckman Coulter) at 80,000 rpm for 10 min at 4°C.

(D1)₂ and iE5 concentrations were estimated by UV absorption using NanoDrop One/OneC (Thermo Fisher Scientific; extinction coefficients: 13,980 and 5,960 $\text{M}^{-1} \text{cm}^{-1}$; molecular weights: 35.2 and 25.1 kD, respectively).

Glass

Polyethylene glycol (PEG)-passivated glass, functionalized with biotin, was prepared as described previously (Consolati et al., 2022). Glass for γ TuRC nucleation assays was generally used within 2 wk; otherwise, glass was generally used within 8 wk.

Stabilized GMPCPP seeds

Stabilized microtubules (seeds) were polymerized using the slowly hydrolyzing GTP analog, GMPCPP (Jena Bioscience). Seeds were polymerized from 3 μM of tubulin in BRB80 (80 mM K-PIPES, 1 mM MgCl_2 , and 1 mM EGTA, pH 6.8; prepared and stored as a 5 \times stock for up to 2 wk), including 18% biotin-labeled tubulin, as well as fluorescent tubulin (AlexaFluor647-NHS or Atto647-NHS) for a final fluorescent labeling ratio of 3–5% for “dim” seeds (used for measurements of seed depolymerization in Fig. 1) or 10–15% for “bright” seeds (used for dynamic assays in Figs. 2 and 3). 200 μl of the tubulin mixture, including 0.5 mM GMPCPP, was incubated on ice for 5 min before transferring to a heat block at 37°C for 1 h to initiate nucleation and elongation. The microtubules were then diluted with 170 μl warm BRB80 and centrifuged at 17,000 $\times g$ for 10 min in a tabletop centrifuge. The microtubule pellet was washed by the addition of 400 μl warm BRB80 and subsequent centrifugation for another 10 min at 17,000 $\times g$ in the tabletop centrifuge. The washed microtubule pellet was finally resuspended in 50 μl warm BRB80. The microtubules were further diluted 100–300-fold in BRB80 at room temperature before microscopy experiments. The microtubules were generally used on the same day. 3 μM of total tubulin resulted in relatively long microtubules, allowing for longer observation times of depolymerization activities, but could be sheared by 10 passes through a 27-gauge needle to generate shorter seeds for shorter seed depolymerization times and therefore more treadmilling events within the experimental timeframe (Fig. 3).

Polarity-marked seeds

To grow microtubules with polarity-marked segments with both segments being stabilized by GMPCPP, we developed a new protocol using the microtubule plus end capping DARPin (D1)₂ (Pecqueur et al., 2012). First, dim seeds (3–5% label ratio, 18% biotin tubulin) were prepared as above. Subsequently, a bright GMPCPP mix (10–15% label ratio, 18% biotin tubulin) was prepared on ice, as above. While incubating the mix on ice, 2 µl of 2.5–5 µM DARPin (D1)₂ (diluted in BRB80) was added to 8 µl of the dim seeds. The bright mix was then diluted 1:1 (to 1.5 µM tubulin, 0.25 mM GMPCPP) and 90 µl of the diluted bright mix was allowed to warm for 60 s at 37°C before adding the 10 µl DARPin (D1)₂/dim seed mixture, resulting in a final DARPin (D1)₂ concentration of 50–100 nM. Bright extensions were allowed to polymerize by incubation for 1 h at 37°C before diluting, spinning, washing, spinning, and resuspending as above, except seeds were diluted 1 in 10 or 1 in 6 from the 50 µl resuspension before experiments.

Correct polarity marking of the marked microtubules was confirmed using a gliding assay: flow chambers were assembled from a poly-(L-lysine)-PEG (SuSoS)-passivated counter glass and an untreated cover glass separated by double-sticky tape. The chamber was washed with 50 µl gliding buffer (BRB80 with 5 mM β-ME, 1 mM ATP, 1 mg ml⁻¹ β-casein) using filter paper to pull the solution through the chamber and incubated for 3 min. Then, the chamber was washed with 50 µl of gliding buffer supplemented with 100 nM of the minus-end-directed motor mCherry-HSET (purified as described in Roostalu et al. (2018)), and incubated a further 3 min. Last, 50 µl of room-temperature gliding buffer supplemented with polarity-marked seeds was flowed into the chamber. Subsequently, the chamber was sealed with silicone vacuum grease and imaged on a confocal microscope. 100% of motile microtubules with one bright and one dim segment moved in the direction of their dim end ($n = 37$ microtubules across two experiments), indicating that the bright end is the minus end, and that our method of marking the ends is effective.

TIRF microscopy experiments

KIF2A gel filtration buffer (without ATP or β-ME) and 5 × BRB80 were prepared and stored at 4°C for a maximum of 2 wk, and supplemented with ATP and β-ME, or diluted appropriately in MilliQ water on each day of the experiments. Buffers were filtered (0.22 µm pore size filters) or ultracentrifuged (80,000 rpm, 10 min, 4°C) and stored on ice for the day (Consolati et al., 2020). Flow chambers were assembled from poly-(L-lysine)-PEG-passivated counter glass, biotin-PEG functionalized cover glass, and double-stick tape, as described elsewhere (Consolati et al., 2022).

The assembled flow chamber was incubated for 10 min with 50 µl 5% Pluronic F-127 (Sigma-Aldrich) in MilliQ water followed by two washes with 50 µl of casein buffer (0.2 mg ml⁻¹ κ-casein [Sigma-Aldrich], diluted in BRB80 or the assay buffer). The chamber was subsequently incubated for 5 min with 50 µl of 50 µg ml⁻¹ of NeutrAvidin (Life Technologies) in casein buffer, followed by two washes with 50 µl of room-temperature BRB80 (seed assays; Figs. 1, 2, and 3) or with 50 µl of cold γTuRC

buffer (γTuRC nucleation assays; Figs. 4 and 5). The chamber was then incubated with 50 µl of biotinylated GMPCPP seeds or 50 µl of γTuRC prediluted in γTuRC buffer to the concentration indicated for each experiment. GMPCPP seeds or γTuRC were allowed to bind to the NeutrAvidin surface for 3–5 min followed by two washes with 50 µl of BRB80-based assay buffer (80 mM PIPES, 60 mM KCl, 5 mM Na-phosphate, 1.1 mM EGTA, 2 mM MgCl₂, 1 mM GTP, 1 mM ATP [pH 7; alternatively, ADP or AMPPNP, pH 7], 5 mM β-ME, 0.15% [wt/vol] methylcellulose [4,000 cP; Sigma-Aldrich], 1% [wt/vol] glucose, and 0.02% [vol/vol] Brij-35). The final experimental mix was then flowed in two steps of 25 µl, with a wait time of 30–60 s between flows, to ensure equilibration of the chamber, and finally sealed with silicone vacuum grease (Obermeier). For the treadmilling experiments, the final assay mix was flowed in on a 33°C heat block to promote growth from small seed fragments in the presence of depolymerase activity. The final experimental mix was prepared on ice: assay buffer supplemented with oxygen scavengers (0.1 mg ml⁻¹ catalase [Sigma-Aldrich], 1 mg ml⁻¹ glucose oxidase [Serva]), either no tubulin (for “seed only” and “γTuRC-mGFP-spastin co-localization” experiments) or 11–22.5 µM of tubulin (containing 3–5% AlexaFluor647, Atto647, or Cy5-labelled tubulin, as indicated, for experiments with dynamically growing microtubules), the different enzymes (KIF2A and mScarlet-KIF2A, 0.5–250 nM, mCherry-MCAK, 5–100 nM, spastin 50 and 100 nM, and/or mGFP-spastin 50 and 100 nM as indicated), and the microtubule end capping proteins (iE5, 2 and 10 µM, and/or (D1)₂, 3 and 15 µM). Their concentrations were altered by predilution in KIF2A gel filtration buffer (for experiments using 1 mM ADP or AMPPNP, KIF2A gel-filtration buffer was prepared with the corresponding nucleotides for diluting the proteins such that residual ATP from the storage buffer amounted to <0.0008 mM). KIF2A, mScarlet-KIF2A, mCherry-MCAK, iE5, (D1)₂, spastin and/or mGFP-spastin dilutions in KIF2A gel-filtration buffer accounted for 10% of the final mix volume; otherwise, the equivalent volume of KIF2A gel-filtration buffer was used instead. The experimental mix was finally centrifuged in a 4°C tabletop centrifuge at 17,000 × *g* for 5 min and the supernatant was recovered and returned to a tube on ice.

Polymerization from the seeds or nucleation from γTuRC was initiated with a temperature shift to 33°C in the TIRF microscope incubator (Okolab) and imaging was started within 2 min from the initial temperature shift. For γTuRC-mGFP-spastin co-localization experiments, images were acquired 5 min after shifting the temperature to 33°C on the TIRF microscope.

TIRF microscopy

Experiments were performed on a TIRF microscope (Cairn Research; Hannabuss et al., 2019) using a 100 × 1.49 NA Nikon Objective lens and an Andor iXon 888 Ultra EMCCD camera (Andor Technology) controlled by MetaMorph software (Molecular Devices). The samples were excited using 360° TIRF illumination (iLas2; Gataca Systems). Time-lapse imaging in multiple colors was performed between 1 frame/5 s and 1 frame/2 s. γTuRC-mBFP-AviTag was imaged every frame (Fig. 4, B, C, I, and J; Fig. 5 A; and Videos 4 and 5) or once every 30 frames (Fig. 5, B and C; and Videos 6 and 7). For the γTuRC-mGFP-

spastin colocalization experiment (Fig. 4 D) stream acquisition of 100 frames in 10 s was performed sequentially for each fluorescence channel. Images were acquired with 300 ms exposure times for all channels (γ TuRC-mBFP-AviTag; 405 nm excitation; mGFP-spastin; 488 nm excitation; mScarlet-KIF2A/mCherry-MCAK, 561 nm; Atto647/AlexaFluor647/Cy5-tubulin, 638 nm). Experiments were observed for 20–30 min. Two or three independent experiments were performed per condition.

TIRF microscopy image processing

Unless otherwise stated, all image processing and analysis were performed using Fiji (Schindelin et al., 2012). Recorded movies were first drift-corrected using the descriptor-based stack registration plug-in, developed by Stephan Preibisch and included with Fiji, using the tubulin channel as the registration channel, and further background-subtracted (rolling ball; 50 pixels) prior to further analysis. To measure speeds and intensities, kymographs (space-time plots) were generated from drift-corrected videos using Fiji. For the γ TuRC single-molecule visualization shown in Fig. 4 C, Fig. 3 A, and Video 5, an average γ TuRC image was generated using the “Z project” function in Fiji. The average projection was then used as a static background merged with the other channels. For the γ TuRC-mGFP-spastin co-localization experiment (Fig. 4 D), γ TuRC and mGFP-spastin images were averaged using the Z project function in Fiji. Tracking arrowheads in Videos 3, 5, and 7 were generated using a published plug-in (Daetwyler et al., 2020).

Seed depolymerization speed

From kymographs of each microtubule, depolymerization speeds were measured manually by drawing a line along the shrinking ends, beginning with the first frame and ending with the last frame before the microtubule detaches or disappears, or the last frame of the video. The speed was calculated from the slope of the line. The shrinking could be directly attributed to minus or plus ends in the case of polarity-marked microtubules, which had brighter minus ends. For the KIF2A concentration series data (Fig. 1 E), the polarity of the microtubule was inferred by the relative speed of the shrinking ends.

End-intensity measurement

Kymographs for end-intensity measurement were cropped to 50 pixels in height (corresponding to 50 frames over 245 s). A segmented line tracing each end of polarity-marked microtubules (visualized in the tubulin channel) was drawn on the kymograph and used to measure the average intensity of mScarlet-KIF2A or mCherry-MCAK localizing to the ends (measured in the mScarlet/mCherry channel). The same measurement was used for 6 pixels outside the microtubule area to account for the local background and for 6 pixels inside the microtubule area of the kymograph to measure the intensity on the lattice. Microtubules to which a large aggregate ($>5\times$ the average end intensity) of mScarlet-KIF2A or mCherry-MCAK bound within measured pixels were excluded from the analysis, and represented a minority of the cases. Intensity measurements for each end and the corresponding lattice measurements were corrected by subtracting the background

measured from that end. The “per end” lattice intensities were then averaged to yield an average lattice intensity representing the whole microtubule and then used to calculate the end intensity ratios. The “raw” intensities (Fig. 1 H) were pooled from experiments done on different days with different laser settings and the average lattice intensity of mScarlet-KIF2A in AMPPNP, also measured on each day, was used to normalize the values.

Microtubule dynamics

Kymographs of dynamic microtubules were used to determine the speeds of growing and shrinking phases, measured and calculated similarly to the depolymerization rates of seeds described above. Only measurements with a non-zero slope (and therefore measurable speed) were included for analysis. Microtubule polarity of dynamic microtubules grown from stabilized seeds was determined by comparison of the relative speeds of growth of the ends and comparison to the growth speeds of control microtubules (growing in the absence of added KIF2A, spastin, or end cappers). For microtubules grown from seeds, the catastrophe frequencies of individual microtubules were calculated as the number of catastrophe events (switching from growth to shrinkage) detected in a kymograph divided by the entire duration of the movie. Only microtubules that showed consistent and measurable dynamics for the entire duration of the movie, as captured by the kymograph, were included in the analysis. For determining catastrophe frequencies of γ TuRC-nucleated microtubules, the lifetime of each microtubule was also measured (from the point of appearance until it disappears in the kymograph) and the catastrophe frequency of an individual microtubule was calculated as the number of catastrophes divided by the microtubule’s lifetime. The reported catastrophe frequencies are averages of catastrophe frequencies of individual microtubules.

Fraction of time in the growth phase

For “typical” microtubule dynamics, stochastic switching events between growing and shrinking phases were determined manually using a custom MATLAB interface to record the time points of switching by clicking with the computer mouse, beginning with the first instance of observed growth and ending with the last frame (bottom row) of the kymograph or the last frame in which the microtubule end could be distinguished. Only kymographs with at least one recorded switching event were used for quantification, in which the sum of the growth event durations (the difference between the first and third, third and fifth recorded time points, and so on) was divided by the total measured duration (the difference between the first and last timepoints).

For lower concentrations of KIF2A (2, 5 nM) and MCAK (5, 10, 20 nM), minus-end growth events were difficult to resolve by eye for many kymographs due to small, fast, and heterogeneous fluctuations closer to the limits of our spatial resolution and frame rate. This precluded using the manual analysis normally performed for the stereotypical, saw-toothed kymographs produced by longer-duration dynamic episodes. Therefore, an automated, custom MATLAB script was used to identify minus ends per frame, producing a trace of growth. Traces were

manually inspected and traces that failed to track the end correctly were discarded before calculating the fraction of growth time. This calculation was performed for each trace by summing the number of frames in which growth was detected over the total number of frames.

γ TuRC-nucleated microtubule analysis

For each nucleation assay, microtubules were counted manually using the “Point tool” in Fiji at six different time points until the end of the video. A microtubule was considered γ TuRC-nucleated if only one end displayed episodes of growth and shrinkage while the other remained capped. At a given time point, the total number of γ TuRC-nucleated microtubules was obtained by adding the newly nucleated microtubules to the total number obtained at the previous time point. This quantification included both γ TuRC-capped and γ TuRC-released microtubules. Each γ TuRC-nucleated microtubule that detached from γ TuRC at any point of the experiment was counted as γ TuRC-released.

Each microtubule that displayed dynamicity at both ends from the first frames of observation was considered a spontaneously nucleated microtubule. The number of spontaneously nucleated microtubules over time was quantified as described above for the γ TuRC-nucleated ones.

A microtubule was considered to be treadmilling when a γ TuRC-released microtubule displayed minus-end depolymerization and a dynamic plus end, such that the microtubule seemed to translocate along the glass surface.

γ TuRC-mGFP-spastin colocalization analysis

For each co-localization experiment, at least five different fields of view were imaged per condition tested. After averaging, fluorescent intensities were measured in the entire field of view using Fiji.

Data plots and errors

All data plots were generated using Microsoft Excel or Prism 9 (GraphPad Software). The variability of the data is represented by the standard error of the mean (SEM) using vertical error bars. In cases where none of the conditions had visible standard error bars, the standard deviation (SD) was used instead to visibly indicate the degree of data variability. It is stated in the figure legends which type of error is plotted.

Online supplemental material

Fig. S1 presents Coomassie-stained gels of the recombinant proteins purified in this study. **Fig. S2** shows depolymerization by KIF2A of non-polarity-marked and polarity-marked stabilized microtubules. **Fig. S3** depicts microtubule nucleation mediated by γ TuRC in the absence and presence of KIF2A. **Fig. S4** shows spastin and mGFP-spastin severase activity of stabilized microtubules. **Video 1** shows the asymmetric depolymerization of stabilized microtubules by KIF2A. **Video 2** shows dynamic microtubules in the presence of the minus-end-selective depolymerase KIF2A. **Video 3** shows KIF2A driving treadmilling of dynamic microtubules. **Video 4** shows γ TuRC-mediated microtubule nucleation in the presence of the depolymerase KIF2A. **Video 5** shows KIF2A-driven treadmilling of γ TuRC-nucleated

microtubules. **Video 6** shows the severing of γ TuRC-nucleated microtubules by the combined action of KIF2A and spastin. **Video 7** shows KIF2A and spastin driving the release and treadmilling of γ TuRC-nucleated microtubules.

Data availability

The data that support the findings of this study are available from the corresponding author upon reasonable request.

Acknowledgments

We thank Benoît Gigant (Université Paris-Saclay, CEA, CNRS, Institute for Integrative Biology of the Cell, Gif-sur-Yvette, France) for providing the α Rep iE5 plasmid, Felix Ruhnnow for microscopy and data analysis support, Maria Gili (Centre for Genomic Regulation, Barcelona Institute of Science and Technology, Barcelona, Spain) for insect cell expression of KIF2A constructs, Johanna Roostalu (The Francis Crick Institute, London, UK) for the design of the MCAK and spastin expression constructs, Raquel Garcia-Castellanos for technical support, and the Cell Services of the Francis Crick Institute for producing large HeLa cell cultures.

This work was supported by the Spanish Ministry of Science and Innovation to the EMBL partnership, the Centro de Excelencia Severo Ochoa and the CERCA Programme of the Generalitat de Catalunya, and by the Francis Crick Institute, which receives its core funding from Cancer Research UK (FC001163), the UK Medical Research Council (FC001163), and the Wellcome Trust (FC001163). C. Brito was supported by EMBO long-term fellowship ALTF-883-2020 and Marie Curie fellowship TuRCReg. T. Surrey acknowledges support from the European Research Council (ERC Synergy Grant, Project 951430) and the Spanish Ministry of Science and Innovation (grant PID2019-108415GB-I00). Open Access funding provided by the Universitat Pompeu Fabra.

Author contributions: G. Henkin, C. Brito, and T. Surrey designed research; G. Henkin, C. Brito, and C. Thomas generated reagents, G. Henkin and C. Brito performed all other experiments and analyzed data; G. Henkin, C. Brito, and T. Surrey wrote the manuscript.

Disclosures: The authors declare no competing interests exist.

Submitted: 5 April 2023

Revised: 27 July 2023

Accepted: 4 August 2023

References

- Akhmanova, A., and M.O. Steinmetz. 2015. Control of microtubule organization and dynamics: Two ends in the limelight. *Nat. Rev. Mol. Cell Biol.* 16:711–726. <https://doi.org/10.1038/nrm4084>
- Akhmanova, A., and M.O. Steinmetz. 2019. Microtubule minus-end regulation at a glance. *J. Cell Sci.* 132:jcs.227850. <https://doi.org/10.1242/jcs.227850>
- Arpag, G., E.J. Lawrence, V.J. Farmer, S.L. Hall, and M. Zanic. 2020. Collective effects of XMAP215, EB1, CLASP2, and MCAK lead to robust microtubule treadmilling. *Proc. Natl. Acad. Sci. USA.* 117:12847–12855. <https://doi.org/10.1073/pnas.2003191117>
- Asenjo, A.B., C. Chatterjee, D. Tan, V. DePaoli, W.J. Rice, R. Diaz-Avalos, M. Silvestry, and H. Sosa. 2013. Structural model for tubulin recognition

- and deformation by kinesin-13 microtubule depolymerases. *Cell Rep.* 3: 759–768. <https://doi.org/10.1016/j.celrep.2013.01.030>
- Atherton, J., K. Jiang, M.M. Stangier, Y. Luo, S. Hua, K. Houben, J.J.E. van Hooft, A.P. Joseph, G. Scarabelli, B.J. Grant, et al. 2017. A structural model for microtubule minus-end recognition and protection by CAMSAP proteins. *Nat. Struct. Mol. Biol.* 24:931–943. <https://doi.org/10.1038/nsmb.3483>
- Bailey, M.E., D.L. Sackett, and J.L. Ross. 2015. Katanin severing and binding microtubules are inhibited by tubulin carboxy tails. *Biophys. J.* 109: 2546–2561. <https://doi.org/10.1016/j.bpj.2015.11.011>
- Barisic, M., G. Rajendraprasad, and Y. Steblyanko. 2021. The metaphase spindle at steady state - mechanism and functions of microtubule poleward flux. *Semin. Cell Dev. Biol.* 117:99–117. <https://doi.org/10.1016/j.semcdb.2021.05.016>
- Benoit, M.P.M.H., A.B. Asenjo, and H. Sosa. 2018. Cryo-EM reveals the structural basis of microtubule depolymerization by kinesin-13s. *Nat. Commun.* 9:1662. <https://doi.org/10.1038/s41467-018-04044-8>
- Berman, A.Y., M. Wiczorek, A. Aher, P.D.B. Olinares, B.T. Chait, and T.M. Kapoor. 2023. A nucleotide binding-independent role for γ -tubulin in microtubule capping and cell division. *J. Cell Biol.* 222:e202204102. <https://doi.org/10.1083/jcb.202204102>
- Bindels, D.S., L. Haarbosch, L. van Weeren, M. Postma, K.E. Wiese, M. Mastop, S. Aumonier, G. Gotthard, A. Royant, M.A. Hink, and T.W. Gadella Jr. 2017. mScarlet: A bright monomeric red fluorescent protein for cellular imaging. *Nat. Methods.* 14:53–56. <https://doi.org/10.1038/nmeth.4074>
- Cameron, L.A., G. Yang, D. Cimini, J.C. Canman, O. Kisurina-Evgenieva, A. Khodjakov, G. Danuser, and E.D. Salmon. 2006. Kinesin 5-independent poleward flux of kinetochore microtubules in PtK1 cells. *J. Cell Biol.* 173: 173–179. <https://doi.org/10.1083/jcb.200601075>
- Campanacci, V., A. Urvoas, T. Consolati, S. Cantos-Fernandes, M. Aumont-Nicaise, M. Valerio-Lepiniec, T. Surrey, P. Minard, and B. Gigant. 2019. Selection and characterization of artificial proteins targeting the tubulin α subunit. *Structure.* 27:497–506.e4. <https://doi.org/10.1016/j.str.2018.12.001>
- Castoldi, M., and A.V. Popov. 2003. Purification of brain tubulin through two cycles of polymerization-depolymerization in a high-molarity buffer. *Protein Expr. Purif.* 32:83–88. [https://doi.org/10.1016/S1046-5928\(03\)00218-3](https://doi.org/10.1016/S1046-5928(03)00218-3)
- Claudiani, P., E. Riano, A. Errico, G. Andolfi, and E.I. Rugarli. 2005. Spastin subcellular localization is regulated through usage of different translation start sites and active export from the nucleus. *Exp. Cell Res.* 309: 358–369. <https://doi.org/10.1016/j.yexcr.2005.06.009>
- Consolati, T., G. Henkin, J. Roostalu, and T. Surrey. 2022. Real-time imaging of single γ TuRC-mediated microtubule nucleation events in vitro by TIRF microscopy. *Methods Mol. Biol.* 2430:315–336. https://doi.org/10.1007/978-1-0716-1983-4_21
- Consolati, T., J. Locke, J. Roostalu, Z.A. Chen, J. Gannon, J. Asthana, W.M. Lim, F. Martino, M.A. Cvetkovic, J. Rappsilber, et al. 2020. Microtubule nucleation properties of single human γ TuRCs explained by their cryo-EM structure. *Dev. Cell.* 53:603–617.e8. <https://doi.org/10.1016/j.devcel.2020.04.019>
- Daetwyler, S., C.D. Modes, and R. Fiolka. 2020. Fiji plugin for annotating movies with custom arrows. *Biol. Open.* 9:bio056200. <https://doi.org/10.1242/bio.056200>
- Desai, A., and T.J. Mitchison. 1997. Microtubule polymerization dynamics. *Annu. Rev. Cell Dev. Biol.* 13:83–117. <https://doi.org/10.1146/annurev.cellbio.13.1.83>
- Desai, A., S. Verma, T.J. Mitchison, and C.E. Walczak. 1999. Kin I kinesins are microtubule-depolymerizing enzymes. *Cell.* 96:69–78. [https://doi.org/10.1016/S0092-8674\(00\)80960-5](https://doi.org/10.1016/S0092-8674(00)80960-5)
- Ems-McClung, S.C., and C.E. Walczak. 2010. Kinesin-13s in mitosis: Key players in the spatial and temporal organization of spindle microtubules. *Semin. Cell Dev. Biol.* 21:276–282. <https://doi.org/10.1016/j.semcdb.2010.01.016>
- Ferenz, N.P., and P. Wadsworth. 2007. Prophase microtubule arrays undergo flux-like behavior in mammalian cells. *Mol. Biol. Cell.* 18:3993–4002. <https://doi.org/10.1091/mbc.e07-05-0420>
- Friel, C.T., and J.P. Welburn. 2018. Parts list for a microtubule depolymerizing kinesin. *Biochem. Soc. Trans.* 46:1665–1672. <https://doi.org/10.1042/BST20180350>
- Gaetz, J., and T.M. Kapoor. 2004. Dynein/dynactin regulate metaphase spindle length by targeting depolymerizing activities to spindle poles. *J. Cell Biol.* 166:465–471. <https://doi.org/10.1083/jcb.200404015>
- Ganem, N.J., and D.A. Compton. 2004. The Kin I kinesin Kif2a is required for bipolar spindle assembly through a functional relationship with MCAK. *J. Cell Biol.* 166:473–478. <https://doi.org/10.1083/jcb.200404012>
- Ganem, N.J., K. Upton, and D.A. Compton. 2005. Efficient mitosis in human cells lacking poleward microtubule flux. *Curr. Biol.* 15:1827–1832. <https://doi.org/10.1016/j.cub.2005.08.065>
- Gardner, M.K., M. Zanin, C. Gell, V. Bormuth, and J. Howard. 2011. Depolymerizing kinesins Kip3 and MCAK shape cellular microtubule architecture by differential control of catastrophe. *Cell.* 147:1092–1103. <https://doi.org/10.1016/j.cell.2011.10.037>
- Goodwin, S.S., and R.D. Vale. 2010. Patronin regulates the microtubule network by protecting microtubule minus ends. *Cell.* 143:263–274. <https://doi.org/10.1016/j.cell.2010.09.022>
- Grego, S., V. Cantillana, and E.D. Salmon. 2001. Microtubule treadmilling in vitro investigated by fluorescence speckle and confocal microscopy. *Biophys. J.* 81:66–78. [https://doi.org/10.1016/S0006-3495\(01\)75680-9](https://doi.org/10.1016/S0006-3495(01)75680-9)
- Guan, C., S. Hua, and K. Jiang. 2023. The CEP170B-KIF2A complex destabilizes microtubule minus ends to generate polarized microtubule network. *EMBO J.* 42:e12953. <https://doi.org/10.15252/emboj.2022112953>
- Gudimchuk, N.B., and J.R. McIntosh. 2021. Regulation of microtubule dynamics, mechanics and function through the growing tip. *Nat. Rev. Mol. Cell Biol.* 22:777–795. <https://doi.org/10.1038/s41580-021-00399-x>
- Guerreiro, A., F. De Sousa, N. Liaudet, D. Ivanova, A. Eskat, and P. Meraldi. 2021. WDR62 localizes katanin at spindle poles to ensure synchronous chromosome segregation. *J. Cell Biol.* 220:e202007171. <https://doi.org/10.1083/jcb.202007171>
- Hannabuss, J., M. Lera-Ramirez, N.I. Cade, F.J. Fourniol, F. Nédélec, and T. Surrey. 2019. Self-organization of minimal anaphase spindle midzone bundles. *Curr. Biol.* 29:2120–2130.e7. <https://doi.org/10.1016/j.cub.2019.05.049>
- Helenius, J., G. Brouhard, Y. Kalaidzidis, S. Diez, and J. Howard. 2006. The depolymerizing kinesin MCAK uses lattice diffusion to rapidly target microtubule ends. *Nature.* 441:115–119. <https://doi.org/10.1038/nature04736>
- Hentrich, C., and T. Surrey. 2010. Microtubule organization by the antagonistic mitotic motors kinesin-5 and kinesin-14. *J. Cell Biol.* 189:465–480. <https://doi.org/10.1083/jcb.200910125>
- Hertzer, K.M., S.C. Ems-McClung, S.L. Kline-Smith, T.G. Lipkin, S.P. Gilbert, and C.E. Walczak. 2006. Full-length dimeric MCAK is a more efficient microtubule depolymerase than minimal domain monomeric MCAK. *Mol. Biol. Cell.* 17:700–710. <https://doi.org/10.1091/mbc.e05-08-0821>
- Huang, J., Z. Liang, C. Guan, S. Hua, and K. Jiang. 2021. WDR62 regulates spindle dynamics as an adaptor protein between TPX2/Aurora A and katanin. *J. Cell Biol.* 220:e202007167. <https://doi.org/10.1083/jcb.202007167>
- Hunter, A.W., M. Caplow, D.L. Coy, W.O. Hancock, S. Diez, L. Wordeman, and J. Howard. 2003. The kinesin-related protein MCAK is a microtubule depolymerase that forms an ATP-hydrolyzing complex at microtubule ends. *Mol. Cell.* 11:445–457. [https://doi.org/10.1016/S1097-2765\(03\)00049-2](https://doi.org/10.1016/S1097-2765(03)00049-2)
- Jiang, K., L. Rezaikkova, S. Hua, Q. Liu, G. Capitani, A.F.M. Altelaar, A.J.R. Heck, R.A. Kammerer, M.O. Steinmetz, and A. Akhmanova. 2017. Microtubule minus-end regulation at spindle poles by an ASPM-katanin complex. *Nat. Cell Biol.* 19:480–492. <https://doi.org/10.1038/ncb3511>
- Kiewisz, R., G. Fabig, W. Conway, D. Baum, D. Needleman, and T. Müller-Reichert. 2022. Three-dimensional structure of kinetochore-fibers in human mitotic spindles. *eLife.* 11:e75459. <https://doi.org/10.7554/eLife.75459>
- Kollman, J.M., A. Merdes, L. Mourey, and D.A. Agard. 2011. Microtubule nucleation by γ -tubulin complexes. *Nat. Rev. Mol. Cell Biol.* 12:709–721. <https://doi.org/10.1038/nrm3209>
- Kuo, Y.W., O. Trottier, M. Mahamdeh, and J. Howard. 2019. Spastin is a dual-function enzyme that severs microtubules and promotes their regrowth to increase the number and mass of microtubules. *Proc. Natl. Acad. Sci. USA.* 116:5533–5541. <https://doi.org/10.1073/pnas.1818824116>
- Laguillo-Diego, A., R. Kiewisz, C. Martí-Gómez, D. Baum, T. Müller-Reichert, and I. Vernos. 2023. MCRS1 modulates the heterogeneity of microtubule minus-end morphologies in mitotic spindles. *Mol. Biol. Cell.* 34:ar1. <https://doi.org/10.1091/mbc.E22-08-0306-T>
- Laycock, J.E., M.S. Savoian, and D.M. Glover. 2006. Antagonistic activities of Klp10A and Orbit regulate spindle length, bipolarity and function in vivo. *J. Cell Sci.* 119:2354–2361. <https://doi.org/10.1242/jcs.02957>
- Maney, T., M. Wagenbach, and L. Wordeman. 2001. Molecular dissection of the microtubule depolymerizing activity of mitotic centromere-associated kinesin. *J. Biol. Chem.* 276:34753–34758. <https://doi.org/10.1074/jbc.M106626200>
- Manning, A.L., N.J. Ganem, S.F. Bakhom, M. Wagenbach, L. Wordeman, and D.A. Compton. 2007. The kinesin-13 proteins Kif2a, Kif2b, and Kif2c/MCAK have distinct roles during mitosis in human cells. *Mol. Biol. Cell.* 18:2970–2979. <https://doi.org/10.1091/mbc.e07-02-0110>
- Margolis, R.L., and L. Wilson. 1978. Opposite end assembly and disassembly of microtubules at steady state in vitro. *Cell.* 13:1–8. [https://doi.org/10.1016/0092-8674\(78\)90132-0](https://doi.org/10.1016/0092-8674(78)90132-0)

- McHugh, T., J. Zou, V.A. Volkov, A. Bertin, S.K. Talapatra, J. Rappaport, M. Dogterom, and J.P.I. Welburn. 2019. The depolymerase activity of MCAK shows a graded response to Aurora B kinase phosphorylation through allosteric regulation. *J. Cell Sci.* 132:jcs228353. <https://doi.org/10.1242/jcs.228353>
- McNally, F.J., K. Okawa, A. Iwamatsu, and R.D. Vale. 1996. Katanin, the microtubule-severing ATPase, is concentrated at centrosomes. *J. Cell Sci.* 109:561–567. <https://doi.org/10.1242/jcs.109.3.561>
- Mitchison, T., and M. Kirschner. 1984. Dynamic instability of microtubule growth. *Nature*. 312:237–242. <https://doi.org/10.1038/312237a0>
- Mitchison, T.J. 1989. Polewards microtubule flux in the mitotic spindle: Evidence from photoactivation of fluorescence. *J. Cell Biol.* 109:637–652. <https://doi.org/10.1083/jcb.109.2.637>
- Montenegro Gouveia, S., K. Leslie, L.C. Kapitein, R.M. Buey, I. Grigoriev, M. Wagenbach, I. Smal, E. Meijering, C.C. Hoogenraad, L. Wordeman, et al. 2010. In vitro reconstitution of the functional interplay between MCAK and EB3 at microtubule plus ends. *Curr. Biol.* 20:1717–1722. <https://doi.org/10.1016/j.cub.2010.08.020>
- Moore, C.A., J. Cooper, M. Wagenbach, Y. Ovechkina, L. Wordeman, and R.A. Milligan. 2006. The role of the kinesin-13 neck in microtubule depolymerization. *Cell Cycle*. 5:1812–1815. <https://doi.org/10.4161/cc.5.16.3134>
- Moore, C.A., and R.A. Milligan. 2006. Lucky 13—microtubule depolymerization by kinesin-13 motors. *J. Cell Sci.* 119:3905–3913. <https://doi.org/10.1242/jcs.03224>
- Moore, C.A., M. Yu, J. Guo, C. Beraud, R. Sakowicz, and R.A. Milligan. 2002. A mechanism for microtubule depolymerization by Kif1 kinesins. *Mol. Cell*. 9:903–909. [https://doi.org/10.1016/S1097-2765\(02\)00503-8](https://doi.org/10.1016/S1097-2765(02)00503-8)
- Moriwaki, T., and G. Goshima. 2016. Five factors can reconstitute all three phases of microtubule polymerization dynamics. *J. Cell Biol.* 215:357–368. <https://doi.org/10.1083/jcb.201604118>
- Pecqueur, L., C. Duellberg, B. Dreier, Q. Jiang, C. Wang, A. Plückthun, T. Surrey, B. Gigant, and M. Knossow. 2012. A designed ankyrin repeat protein selected to bind to tubulin caps the microtubule plus end. *Proc. Natl. Acad. Sci. USA*. 109:12011–12016. <https://doi.org/10.1073/pnas.1204129109>
- Rai, D., S. Hua, J.L. Monster, R. Stucchi, K. Stecker, Y. Zhang, E.A. Katrukha, M. Altaar, M. Wiczorek, K. Jiang, et al. 2022. CAMSAP-driven microtubule release from γ -TuRC and its regulation by nucleation-promoting factors. *bioRxiv*. <https://doi.org/10.1101/2022.08.03.502613> (Preprint posted August 3, 2022).
- Rath, U., G.C. Rogers, D. Tan, M.A. Gomez-Ferrera, D.W. Buster, H.J. Sosa, and D.J. Sharp. 2009. The *Drosophila* kinesin-13, KLP59D, impacts Pacman- and Flux-based chromosome movement. *Mol. Biol. Cell*. 20:4696–4705. <https://doi.org/10.1091/mbc.e09-07-0557>
- Risteski, P., D. Božan, M. Jagrić, A. Bosilj, N. Pavin, and I.M. Tolić. 2022. Length-dependent poleward flux of sister kinetochore fibers promotes chromosome alignment. *Cell Rep.* 40:111169. <https://doi.org/10.1016/j.celrep.2022.111169>
- Rodionov, V.I., and G.G. Borisy. 1997. Microtubule treadmilling in vivo. *Science*. 275:215–218. <https://doi.org/10.1126/science.275.5297.215>
- Rogers, G.C., S.L. Rogers, T.A. Schwimmer, S.C. Ems-McClung, C.E. Walczak, R.D. Vale, J.M. Scholey, and D.J. Sharp. 2004. Two mitotic kinesins cooperate to drive sister chromatid separation during anaphase. *Nature*. 427:364–370. <https://doi.org/10.1038/nature02256>
- Rogers, G.C., S.L. Rogers, and D.J. Sharp. 2005. Spindle microtubules in flux. *J. Cell Sci.* 118:1105–1116. <https://doi.org/10.1242/jcs.02284>
- Roll-Mecak, A., and R.D. Vale. 2005. The *Drosophila* homologue of the hereditary spastic paraplegia protein, spastin, severs and disassembles microtubules. *Curr. Biol.* 15:650–655. <https://doi.org/10.1016/j.cub.2005.02.029>
- Roll-Mecak, A., and R.D. Vale. 2008. Structural basis of microtubule severing by the hereditary spastic paraplegia protein spastin. *Nature*. 451:363–367. <https://doi.org/10.1038/nature06482>
- Roostalu, J., J. Rickman, C. Thomas, F. Nédélec, and T. Surrey. 2018. Determinants of polar versus nematode organization in networks of dynamic microtubules and mitotic motors. *Cell*. 175:796–808.e14. <https://doi.org/10.1016/j.cell.2018.09.029>
- Schaedel, L., K. John, J. Gaillard, M.V. Nachury, L. Blanchoin, and M. Théry. 2015. Microtubules self-repair in response to mechanical stress. *Nat. Mater.* 14:1156–1163. <https://doi.org/10.1038/nmat4396>
- Schindelin, J., I. Arganda-Carreras, E. Frise, V. Kaynig, M. Longair, T. Pietzsch, S. Preibisch, C. Rueden, S. Saalfeld, B. Schmid, et al. 2012. Fiji: An open-source platform for biological-image analysis. *Nat. Methods*. 9:676–682. <https://doi.org/10.1038/nmeth.2019>
- Shaner, N.C., R.E. Campbell, P.A. Steinbach, B.N. Giepmans, A.E. Palmer, and R.Y. Tsien. 2004. Improved monomeric red, orange and yellow fluorescent proteins derived from *Discosoma* sp. red fluorescent protein. *Nat. Biotechnol.* 22:1567–1572. <https://doi.org/10.1038/nbt1037>
- Sharp, D.J., and J.L. Ross. 2012. Microtubule-severing enzymes at the cutting edge. *J. Cell Sci.* 125:2561–2569. <https://doi.org/10.1242/jcs.101139>
- Shaw, S.L., R. Kamyar, and D.W. Ehrhardt. 2003. Sustained microtubule treadmilling in *Arabidopsis* cortical arrays. *Science*. 300:1715–1718. <https://doi.org/10.1126/science.1083529>
- Steblyanko, Y., G. Rajendraprasad, M. Osswald, S. Eibes, A. Jacome, S. Geley, A.J. Pereira, H. Maiato, and M. Barisic. 2020. Microtubule poleward flux in human cells is driven by the coordinated action of four kinesins. *EMBO J.* 39:e105432. <https://doi.org/10.15252/embj.2020105432>
- Tan, D., A.B. Asenjo, V. Mennella, D.J. Sharp, and H. Sosa. 2006. Kinesin-13s form rings around microtubules. *J. Cell Biol.* 175:25–31. <https://doi.org/10.1083/jcb.200605194>
- Tan, D., W.J. Rice, and H. Sosa. 2008. Structure of the kinesin13-microtubule ring complex. *Structure*. 16:1732–1739. <https://doi.org/10.1016/j.str.2008.08.017>
- Thawani, A., M.J. Rale, N. Coudray, G. Bhabha, H.A. Stone, J.W. Shaevitz, and S. Petry. 2020. The transition state and regulation of γ -TuRC-mediated microtubule nucleation revealed by single molecule microscopy. *eLife*. 9:e54253. <https://doi.org/10.7554/eLife.54253>
- Tovey, C.A., and P.T. Conduit. 2018. Microtubule nucleation by γ -tubulin complexes and beyond. *Essays Biochem.* 62:765–780. <https://doi.org/10.1042/EBC20180028>
- Trofimova, D., M. Paydar, A. Zara, L. Talje, B.H. Kwok, and J.S. Allingham. 2018. Ternary complex of Kif2A-bound tandem tubulin heterodimers represents a kinesin-13-mediated microtubule depolymerization reaction intermediate. *Nat. Commun.* 9:2628. <https://doi.org/10.1038/s41467-018-05025-7>
- Uehara, R., Y. Tsukada, T. Kamasaki, I. Poser, K. Yoda, D.W. Gerlich, and G. Goshima. 2013. Aurora B and Kif2A control microtubule length for assembly of a functional central spindle during anaphase. *J. Cell Biol.* 202:623–636. <https://doi.org/10.1083/jcb.201302123>
- Vale, R.D. 1991. Severing of stable microtubules by a mitotically activated protein in *Xenopus* egg extracts. *Cell*. 64:827–839. [https://doi.org/10.1016/0092-8674\(91\)90511-V](https://doi.org/10.1016/0092-8674(91)90511-V)
- Vemu, A., E. Szczesna, E.A. Zehr, J.O. Spector, N. Grigorieff, A.M. Deaconescu, and A. Roll-Mecak. 2018. Severing enzymes amplify microtubule arrays through lattice GTP-tubulin incorporation. *Science*. 361:eaau1504. <https://doi.org/10.1126/science.aau1504>
- Wang, W., S. Cantos-Fernandes, Y. Lv, H. Kuerban, S. Ahmad, C. Wang, and B. Gigant. 2017. Insight into microtubule disassembly by kinesin-13s from the structure of Kif2C bound to tubulin. *Nat. Commun.* 8:70. <https://doi.org/10.1038/s41467-017-00091-9>
- Waterman-Storer, C.M., and E.D. Salmon. 1997. Actomyosin-based retrograde flow of microtubules in the lamella of migrating epithelial cells influences microtubule dynamic instability and turnover and is associated with microtubule breakage and treadmilling. *J. Cell Biol.* 139:417–434. <https://doi.org/10.1083/jcb.139.2.417>
- Welburn, J.P., and I.M. Cheeseman. 2012. The microtubule-binding protein Cep170 promotes the targeting of the kinesin-13 depolymerase Kif2b to the mitotic spindle. *Mol. Biol. Cell*. 23:4786–4795. <https://doi.org/10.1091/mbc.e12-03-0214>
- Wiczorek, M., S.C. Ti, L. Urnavicius, K.R. Molloy, A. Aher, B.T. Chait, and T.M. Kapoor. 2021. Biochemical reconstitutions reveal principles of human γ -TuRC assembly and function. *J. Cell Biol.* 220:e202009146. <https://doi.org/10.1083/jcb.202009146>
- Wilbur, J.D., and R. Heald. 2013. Mitotic spindle scaling during *Xenopus* development by kif2a and importin α . *eLife*. 2:e00290. <https://doi.org/10.7554/eLife.00290>
- Wordeman, L., M. Wagenbach, and G. von Dassow. 2007. MCAK facilitates chromosome movement by promoting kinetochore microtubule turnover. *J. Cell Biol.* 179:869–879. <https://doi.org/10.1083/jcb.200707120>
- Zehr, E.A., A. Szyk, E. Szczesna, and A. Roll-Mecak. 2020. Katanin grips the β -tubulin tail through an electropositive double spiral to sever microtubules. *Dev. Cell*. 52:118–131.e6. <https://doi.org/10.1016/j.devcel.2019.10.010>
- Zhang, D., A.B. Asenjo, M. Greenbaum, L. Xie, D.J. Sharp, and H. Sosa. 2013. A second tubulin binding site on the kinesin-13 motor head domain is important during mitosis. *PLoS One*. 8:e73075. <https://doi.org/10.1371/journal.pone.0073075>
- Zhang, D., G.C. Rogers, D.W. Buster, and D.J. Sharp. 2007. Three microtubule severing enzymes contribute to the “Pacman-flux” machinery that moves chromosomes. *J. Cell Biol.* 177:231–242. <https://doi.org/10.1083/jcb.200612011>

Supplemental material

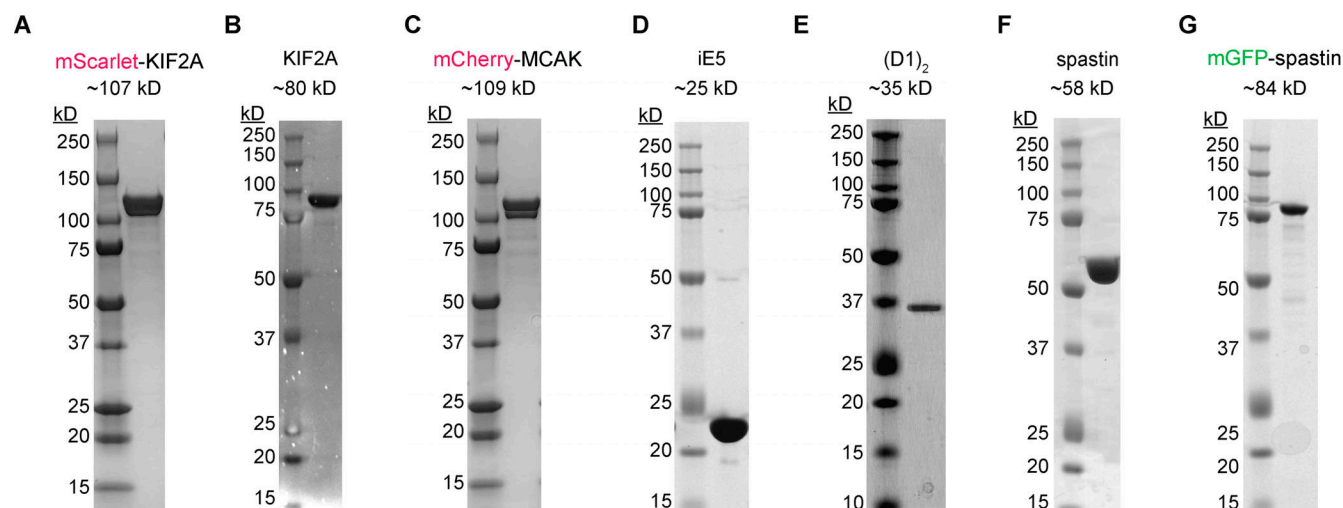


Figure S1. **Coomassie-stained SDS gel with purified recombinant proteins used in this study.** (A–G) mScarlet KIF2A (A); untagged KIF2A (B); mCherry-MCAK (C); iE5 (D); (D1)₂ (E); spastin (F); and mGFP-spastin (G). mCherry-tagged proteins migrate as double bands, as previously published (Hentrich and Surrey, 2010; Roostalu et al., 2018), possibly associated with different maturation states of mCherry. mScarlet, derived from mCherry (Bindels et al., 2017), causes a similar migration pattern. Source data are available for this figure: SourceData F51.

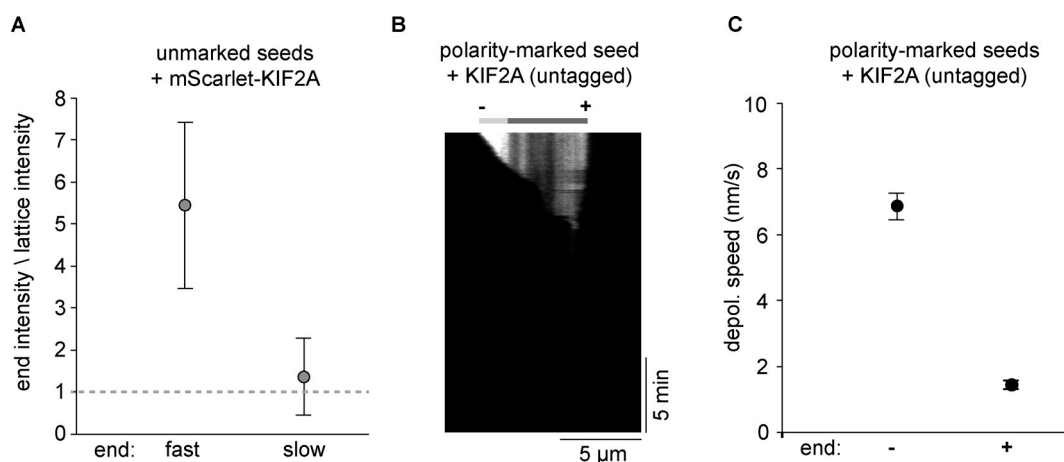


Figure S2. **Depolymerization of non-polarity-marked and polarity-marked GMPCPP microtubules by KIF2A.** (A) Ratio of intensities of mScarlet-KIF2A at the fast and slowly growing ends of non-polarity-marked microtubules to its intensity on the microtubule lattice (see Materials and methods). Measurements made from $n = 27$ microtubules. Error bars are SEM. (B) Example kymograph demonstrating the minus-end selectivity of KIF2A depolymerizing a polarity-marked GMPCPP microtubule. Polarity as indicated. (C) Depolymerization speeds of minus and plus ends of polarity-marked microtubules in the presence of 20 nM untagged KIF2A. Measurements were made from $n = 69$ microtubules. Error bars are SEM.

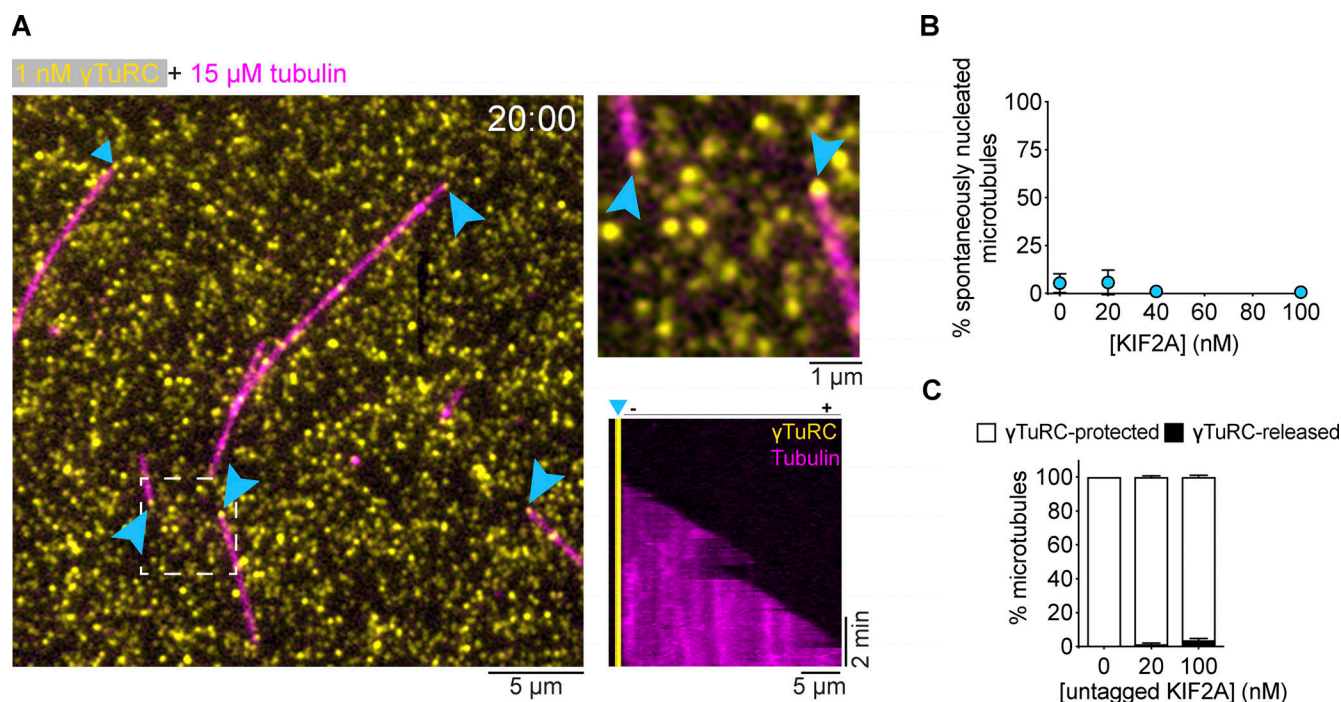


Figure S3. **γ TuRC-nucleated microtubules in the absence and presence of KIF2A.** (A) Left: TIRF microscopy snapshot of single γ TuRC-nucleated microtubules (magenta) 20 min after the start of imaging in the presence of 15 μ M tubulin (AlexaFluor647, 5.4%). 1 nM biotinylated and BFP-tagged γ TuRC (yellow) was used for immobilization. γ TuRC signal is an average of all frames imaged during 20 min (right, top). The inset of the dashed area shows two γ TuRC-capped microtubules. γ TuRC-mediated nucleation sites are indicated by cyan arrows. Right, bottom: Kymograph showing microtubule (magenta) minus-end capping by γ TuRC (yellow) and a dynamic plus end. (B) Plot of the percentage of spontaneously nucleated microtubules in solution in γ TuRC nucleation assays using 12.5 μ M of tubulin and different mScarlet-KIF2A (cyan) concentrations, as indicated. Number of microtubules analyzed per condition: 0 nM, $n = 256$; 20 nM, $n = 249$; 40 nM, $n = 190$; 100 nM, $n = 91$. Data for plots were pooled from three independent experiments. Error bars are SEM. For symbols without visible error bars, error bars are smaller than the symbol size. (C) Bar graph of the mean percentage of microtubules that either remain protected by γ TuRC or are released after nucleation in the presence of the indicated concentrations of untagged KIF2A. Number of microtubules analyzed per condition: 0 nM, $n = 162$; 20 nM, $n = 199$; 100 nM, $n = 83$; Data for plots were pooled from at least two independent experiments. Error bars are SEM. 2 nM of γ TuRC was used for immobilization in B and C.

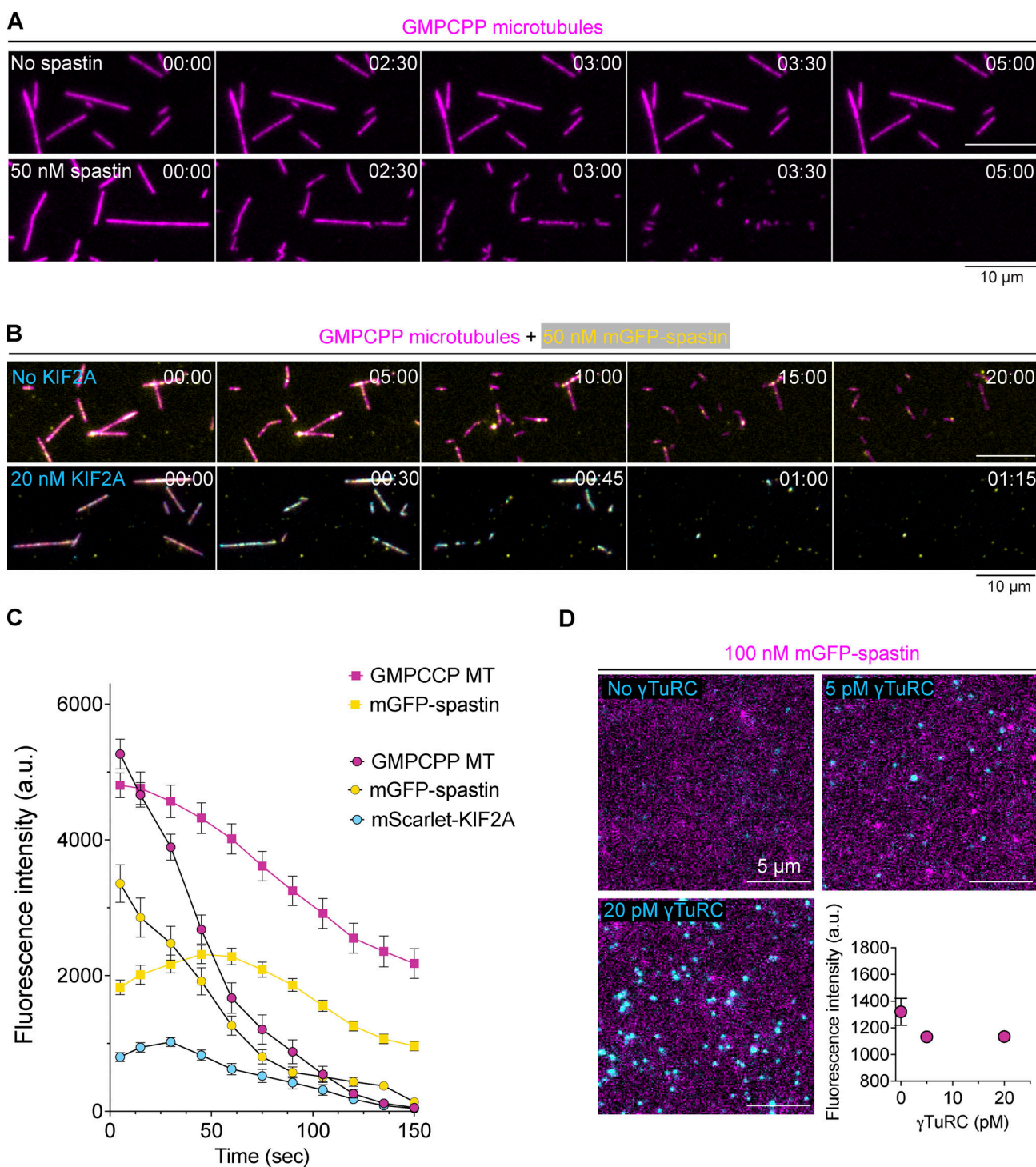


Figure S4. Severing of stabilized microtubule seeds by the severase spastin and mGFP-spastin. **(A)** Time sequence of TIRF microscopy images of immobilized GMPCPP microtubules (AlexaFluor647 5%, magenta) in the absence or presence of 50 nM of spastin. **(B)** Time sequence of TIRF microscopy images of immobilized GMPCPP microtubules (Atto647 5%, magenta) and mGFP-spastin (yellow) in the absence or presence of 20 nM of mScarlet-KIF2A (cyan). Time in B and C is min:s. **(C)** Time course of fluorescence intensities of GMPCPP microtubules (magenta), mGFP-spastin (yellow), and mScarlet-KIF2A (cyan) measured along the initial contour of microtubules in the presence of 50 nM mGFP-spastin (squares) or 50 nM mGFP-spastin and 20 nM KIF2A (circles). Number of microtubules analyzed per condition: 50 nM mGFP-spastin, $n = 81$; 50 nM mGFP-spastin and 20 nM KIF2A, $n = 87$. Data for plots were pooled from at least two independent experiments. Error bars are SEM. For symbols without visible error bars, error bars are smaller than the symbol size. **(D)** TIRF microscopy images of 100 nM mGFP-spastin in the absence or presence of immobilized γ TuRC. γ TuRC concentrations were used for immobilization as indicated. The fluorescence intensities of mGFP-spastin (bottom, right; see Materials and methods) represent the background intensity and are independent of the γ TuRC density on the surface, demonstrating the absence of interaction between γ TuRC and spastin. Moreover, no colocalization is observed, also indicating absence of interaction. Data for plots were pooled from at least two independent experiments. Error bars are SEM. For symbols without visible error bars, error bars are smaller than the symbol size.

Video 1. **Asymmetric depolymerization of stabilized microtubules by KIF2A.** GMPCPP-stabilized microtubules (magenta) undergoing depolymerization in the presence of 20 nM mScarlet-KIF2A (cyan). Scale bar, 5 μ m. Related to [Fig. 1](#).

Video 2. **Minus-end-selective depolymerization of dynamic microtubules by KIF2A.** Dynamic microtubules (magenta) growing from brightly labeled GMPCPP seeds in the presence of 12.5 μ M tubulin, 2 nM (top), and 20 nM (bottom) mScarlet-KIF2A. Scale bar, 5 μ m. Related to [Fig. 2](#).

Video 3. **KIF2A drives treadmilling of dynamic microtubules.** Treadmilling microtubules growing in the presence of 22.5 μ M tubulin from brightly labeled GMPCPP seeds (magenta) in the presence of 20 nM mScarlet-KIF2A (cyan). Yellow arrows track depolymerizing minus ends of selected treadmilling microtubules. Scale bar, 5 μ m. Related to [Fig. 3](#).

Video 4. **KIF2A decreases γ TuRC-mediated microtubule nucleation.** Microtubules (magenta) nucleated from surface-immobilized γ TuRC in the presence of 12.5 μ M tubulin and mScarlet-KIF2A (cyan), at the indicated concentrations. Scale bar, 10 μ m. Video corresponding to [Fig. 4 B](#).

Video 5. **KIF2A-driven treadmilling event of a γ TuRC-nucleated microtubule.** Microtubule (magenta) nucleated from surface-immobilized γ TuRC (yellow) in the presence of 12.5 μ M tubulin and 20 nM of mScarlet-KIF2A (cyan). After γ TuRC-mediated microtubule nucleation, in very rare cases, KIF2A disrupts the γ TuRC-microtubule interface, triggering microtubule release and subsequent treadmilling. The white arrowhead follows the microtubule minus ends. Scale bar, 5 μ m. Video related to [Fig. 4, H and J](#).

Video 6. **γ TuRC-nucleated microtubules are severed when KIF2A and spastin act in synergy.** Severing of γ TuRC-nucleated microtubules (magenta) in the presence of 11 μ M tubulin, 100 nM of spastin, and 20 nM of mScarlet-KIF2A (cyan). Scale bars, 2 μ m. Video corresponds to [Fig. 5 B](#).

Video 7. **KIF2A and spastin drive the release and treadmilling of γ TuRC-nucleated microtubules.** Microtubules (magenta) nucleated from surface-immobilized γ TuRC in the presence of 11 μ M tubulin, 100 nM spastin, and 20 nM of mScarlet-KIF2A (cyan). After γ TuRC-mediated microtubule nucleation, microtubule release and subsequent treadmilling is triggered by the combined action of spastin and KIF2A. The yellow arrowheads point to the minus ends of the microtubules. Scale bar, 2 μ m. Video corresponds to [Fig. 5 C](#).